

ENDO-LYSOSOME-TARGETED NANOPARTICLE DELIVERY OF ANTIVIRAL THERAPY FOR CORONAVIRUS INFECTIONS

Short Title: Antiviral nanoparticles as a coronavirus treatment

Anton Petcherski^{1*}, Brett M Tingley^{2*}, Andrew Martin², Sarah Adams², Alexandra J Brownstein^{1,3}, Ross A Steinberg¹, Byourak Shabane¹, Gustavo Garcia Jr⁴, Michaela Veliova^{1,4}, Vaithilingaraja Arumugaswami⁴, Aaron H Colby², Orian S Shirihai^{1,4#}, and Mark W Grinstaff^{2,5#}

¹ Department of Medicine, Division of Endocrinology, David Geffen School of Medicine, University of California Los Angeles, Los Angeles, CA, USA

² Department of Biomedical Engineering, Boston University, Boston, MA, USA

³ Molecular Cellular Integrative Physiology, University of California Los Angeles, Los Angeles, CA, USA

⁴ Department of Molecular and Medical Pharmacology, David Geffen School of Medicine, University of California Los Angeles, Los Angeles, CA, USA

⁵ Department of Chemistry, Boston University, Boston, MA, USA

*co-first

#co-corresponding

SUMMARY

SARS-CoV-2 can infect cells through endocytic uptake, a process which can be targeted by inhibition of lysosomal proteases. However, clinically this approach fared poorly with an oral regimen of hydroxychloroquine that was accompanied by significant toxicity due to off-target effects. We rationalized that an organelle-targeted approach will avoid toxicity while increasing the concentration of the drug at the target. Here we describe a lysosome-targeted, mefloquine-loaded poly(glycerol monostearate-co- ϵ -caprolactone) nanoparticle (MFQ-NP) for pulmonary delivery via inhalation. Mefloquine is a more effective inhibitor of viral endocytosis than hydroxychloroquine in cellular models of COVID-19. MFQ-NPs are less toxic than molecular mefloquine, 100-150 nm in diameter, and possess a negative surface charge which facilitates uptake via endocytosis allowing inhibition of lysosomal proteases. MFQ-NPs inhibit coronavirus infection in mouse MHV-A59 and human OC43 coronavirus model systems and inhibit SARS-CoV-2-WA1 and its Omicron variant in a human lung epithelium model. This study demonstrates that organelle-targeted delivery is an effective means to inhibit viral infection.

KEYWORDS

COVID-19, SARS-CoV-2, mefloquine, nanoparticles, lysosomes, endocytosis

INTRODUCTION

To date, severe acute respiratory syndrome coronavirus 2 (SARS-CoV-2) has infected over 763 million individuals resulting in over 6.9 million deaths globally, causing significant harm to public health and resulting in a sizable humanitarian and socioeconomic burden (Nicola et al., 2020; WHO, 2023). To combat this crisis, Pfizer and Moderna, among others, developed highly efficacious vaccines (BNT162b2 and mRNA-1273, respectively) at unprecedented speeds which display >94% efficacy in preventing COVID-19 illness, including severe disease (Baden et al., 2021; Polack et al., 2020). Despite rapid development, global distribution of vaccines remains slow, and the virus continues to gain genetic mutations in regions that have been targeted by recently developed prophylactics and treatments. Consequently, neutralization-resistant SARS-CoV-2 variants continue to spike worldwide case numbers and mortality (Dong et al., 2020; Garcia-Beltran et al., 2021).

Concurrently with vaccine development, multiple clinically approved drugs were rapidly repurposed to treat COVID-19 patients (Serafin et al., 2020). These include antimalarial agents such as chloroquine/hydroxychloroquine (CQ/HCQ), protease inhibitors such as lopinavir/ritonavir (LPV/RTV), and viral transcription inhibitors such as remdesivir (RDV). Despite encouraging *in vitro* reports, the clinical use of CQ/HCQ and LPV/RTV for patients with COVID-19 resulted in minimal or no clinical benefit over the standard of care (Cao et al., 2020; Group, 2020; Horby et al., 2020; Patel et al., 2021; WHO, 2021). Clinical trials evaluating RDV afforded mixed outcomes wherein RDV was superior to placebo in shortening the time to recovery in adults who were hospitalized with mild-to-severe COVID-19 in three randomized, controlled clinical trials (Beigel et al., 2020; Goldman et al., 2020; Spinner et al., 2020) but failed to demonstrate improved clinical outcomes as indicated by mortality rates, initiation of ventilation, and total duration of hospital stay in both the WHO Solidarity trial and DisCoVeRy trial (Ader et al., 2022; WHO, 2021). Emerging evidence suggests that RDV improves clinical outcomes, but only if administered within an early time window after infection (Gottlieb et al., 2022; Heil and Kottlil, 2022).

In addition to the early use of repurposed drugs, novel post-exposure prophylaxis and therapeutic candidates have been in development and were FDA-approved. Multiple pharmaceutical companies developed recombinant monoclonal antibodies (mAbs) or noncompeting mAb cocktails to target the receptor binding domain (RBD) on the SARS-CoV-2 S protein, including: Casirivimab and Imdevimab (REGN-COV2), Bamlanivimab and Etesevimab (LY-CoV555 or LY3819253 and LY-CoV016 or LY3832479), and Sotrovimab (VIR-7831). These neutralizing mAbs demonstrated a reduction in viral load in post-exposure prophylaxis in clinical trials and led to a lower incidence of COVID-19 related hospitalization and mortality when treating non-hospitalized patients with COVID-19 (Baum et al., 2020; Dougan et al., 2021; Gottlieb et al., 2021; Gupta et al., 2021; Gupta et al., 2022; Weinreich et al., 2021a; Weinreich et al., 2021b). Despite all three therapies originally receiving emergency use authorization (EUA) from the FDA for treatment and/or post-exposure prophylaxis of COVID-19, due to the high frequency of the emerging Omicron variant, all three are no longer authorized for use in any U.S. region.

Furthermore, other small molecule viral inhibitors were developed such as nirmatrelvir (Pfizer, Paxlovid) and Molnupiravir (Merck), which received FDA approval a year after RDV. Nirmatrelvir is an orally bioavailable viral 3CL^{pro} inhibitor used in combination with ritonavir to slow the metabolism of the drug

(Owen et al., 2021). In a randomized, controlled trial for unvaccinated, non-hospitalized adults at high risk for progression to severe COVID-19, Paxlovid decreased the risk of progression to severe symptoms by 89% over placebo as determined by hospitalization rate and mortality (Hammond et al., 2022). More recently, Pfizer terminated the EPIC-SR trial (NCT05011513) as Paxlovid displayed no clinical benefit over placebo with regard to COVID-19 symptom relief in non-hospitalized symptomatic adults who are at low risk of progressing to severe illness. Additionally, further *in vitro* testing in both a live SARS-CoV-2 and vesicular stomatitis virus (VSV)-based pseudo-virus model suggest that selective pressure may lead to 3CL^{pro} mutations conferring nirmatrelvir resistance to new viral mutants (Heilmann et al., 2022; Jochmans et al., 2022). Molnupiravir is a prodrug nucleoside analog which causes the accumulation of significant point mutations in replicated viral transcripts (Kabinger et al., 2021). In a randomized, controlled trial for non-hospitalized, unvaccinated adults with mild-to-moderate COVID-19 symptoms, early treatment (within 5 days of symptom onset) with Molnupiravir resulted in a significant reduction in risk of hospitalization as well as mortality (Jayk Bernal et al., 2022). However, there is a growing concern that Molnupiravir, especially when administered at sub therapeutic doses, may result in the creation of more virulent SARS-CoV-2 mutants (Agostini et al., 2019). The discrepancy between experimental results and clinical outcomes for early COVID-19 candidates and the potential for neutralization-resistant mutants or creation of more virulent strains from emerging COVID-19 therapies necessitates the development of new strategies, therapeutics, and prophylactics against COVID-19, as well as delivery systems to target the virus or host cell while minimizing off-target toxicity.

There are several small molecule drugs which were also repurposed for the treatment of coronaviruses and indicated efficacy in preclinical models, however they have not gained as much traction as CQ/HCQ and lopinavir. Nitazoxanide is a member of the thiazolide drug class, which are broad-spectrum anti-infection drugs, and shows early promise in both *in vitro* and small-scale *in vivo* trials (Blum et al., 2021; Mahmoud et al., 2020; Wang et al., 2020). The antiviral mechanism of action is not fully characterized, although reports suggest that nitazoxanide may target multiple stages of the SARS-CoV-2 life cycle, including endocytosis and membrane fusion, viral genome synthesis and viral protein processing, and the late stage inflammatory response (Lokhande and Devarajan, 2021). Sulfadoxine is a sulfonamide, which are a class of drugs that are known to interrupt the synthesis of folic acid. Several *in vitro* reports demonstrate anti-SARS-CoV-2 activity with sulfadoxine, although it is unclear if folic acid synthesis plays a role in viral replication or if sulfadoxine has a novel unknown inhibitory action (Arshad et al., 2020; Touret et al., 2020). Mefloquine (MFQ), a 4-quinolinemethanol similar in structure to CQ/HCQ, shows improved activity against SARS-CoV-2 over CQ/HCQ (Sacramento et al., 2022; Shionoya et al., 2021). CQ/HCQ blocks SARS-CoV-2 entry only in cells lacking transmembrane serine protease 2 (TMPRSS2), whereas expression of TMPRSS2 significantly reduces the antiviral activity of CQ/HCQ (Hoffmann et al., 2020; Lee et al., 2021). Unlike CQ/HCQ, MFQ reduces viral load in clinically relevant cell lines, including Calu-3 and Vero E6/TMPRSS2 cells, which express both angiotensin converting enzyme 2 (ACE2) and TMPRSS2 (Sacramento et al., 2022; Shionoya et al., 2021). Thus, MFQ is more broadly active against coronaviruses as compared to CQ/HCQ, and this dependence on the lack of TMPRSS2 may explain the discrepancy between *in vitro* and *in vivo* results reported using CQ/HCQ for the treatment of SARS-CoV-2.

Pharmacokinetic (PK) modeling and analysis further suggests that CQ/HCQ does not achieve therapeutic anti-SARS-CoV-2 concentrations *in vivo* when delivered orally (Liu et al., 2020; McLachlan et al., 1993; Touret et al., 2020). Moreover, multiple clinical trials assessing CQ/HCQ for the treatment of hospitalized patients with COVID-19 displayed an increased risk of drug-induced cardiac toxicities (Tleyjeh et al., 2021). Similar PK modeling of oral MFQ dosing predicts that plasma concentrations above the target EC₉₀ can be achieved only with high doses over multiple days (e.g. 450 mg TID or 350 mg QID for 3 days) which may lead to off-target effects (Karbwan and White, 1990; Sacramento et al., 2022; Shionoya et al., 2021). In fact, prophylactic use of mefloquine for malaria prevention is known to cause neurotoxicity/neurological adverse events (e.g., abnormal dreams, insomnia, anxiety, depressed mood, nausea, dizziness, and chronic central nervous system toxicity syndrome), however the mechanisms underlying its neurotoxic effects are poorly understood (Martins et al., 2021; McCarthy, 2015).

The non-specific delivery route for these small molecules (e.g., oral or intravenous) results in the administration of high doses with low drug accumulation in the target tissue (i.e., the lungs). As many of these small molecules are acutely cytotoxic beyond their therapeutic window, these high doses also lead to significant, off-target effects in tissues not infected with virus. To address the unmet need for a potent antiviral treatment for coronaviruses that locally targets the pulmonary system, we describe nanoparticles based on biocompatible components and loaded with chloroquine, mefloquine, sulfadoxine, or nitazoxanide. The particles are composed of poly(glycerol monostearate-co- ϵ -caprolactone) (PGC-C18), and, of these four payloads, mefloquine-loaded nanoparticles exhibit the strongest inhibitory effect on coronavirus infection. Herein, we report on negatively charged PGC-C18 nanoparticles (NPs) of 100-150 nm in diameter which physically entrap MFQ. MFQ-loaded NPs (MFQ-NPs) are rapidly taken up by cells, localize to endo-lysosomal compartments, and decrease protease activity. MFQ-NPs inhibit coronavirus infection in mouse MHV-A59 and human coronavirus OC43 model systems as well as inhibit SARS-CoV-2-WT and Omicron variant infection in a human lung epithelium cell line model.

RESULTS

PGC-C18 nanoparticle formation and characterization studies

First, we developed a method to prepare nanoparticles (NPs) with a spherical morphology of ~100 nm. Polymeric NPs on this scale are amenable to delivery via inhalation and uptake by endocytosis (Geiser and Kreyling, 2010; Löndahl et al., 2014; Thorley et al., 2014). We selected poly(glycerol monostearate-co- ϵ -caprolactone), PGC-C18 (Fig. 1A), as it is comprised of biocompatible degradation products of glycerol, CO₂, stearate, and 6-Hydroxyhexanoic acid, and we have a large-scale GMP-compatible synthetic method for producing it, which would be useful in speeding clinical translation (Kaplan et al., 2016). To synthesize the polymer, we copolymerized ϵ -caprolactone and 5-benzyloxy-1,3-dioxan-2-one monomers via ring opening polymerization catalyzed by tin(II) 2-ethylhexanoate (Sn(Oct)₂). We subsequently removed the benzyl-protecting groups of poly(5-benzyloxy-1,3-dioxan-2-one-co- ϵ -caprolactone) (PGC-Bn) via palladium-catalyzed hydrogenolysis and conjugated stearic acid to the newly exposed hydroxyl groups via a dicyclohexylcarbodiimide (DCC) coupling. Post-coupling, we confirmed the polymer structure via ¹H NMR (Supp. Fig. 1A, B), and gel permeation chromatography (GPC) analysis with THF as eluent and

polystyrene as standards reveals a molecular weight (M_n) of 78,300 g/mol with narrow dispersity ($\mathcal{D}=1.67$) (Supp. Fig. 1C).

We prepared drug-loaded NPs via the solvent evaporation method (Ekladius et al., 2017) using sodium dodecyl sulfate as the surfactant to stabilize the formation of spherical nanoparticles containing a core of PGC-C18 polymer encapsulating a hydrophobic drug payload (Fig. 1B). SEM analysis of NP structure and size reveals spherical NPs of ~ 100 nm diameter (Fig. 1C). Quantitative analysis using dynamic light scattering (DLS) confirms the size range of 100-150 nm with a good uniformity reflected in a polydispersity index of < 0.17 (Fig. 1D). Additionally, NP surface charge, as analyzed by DLS, is highly negative with a zeta-potential of ≤ -30 mV in unloaded and drug-loaded NPs (Fig. 1E), which imparts NP stability (Ekladius et al., 2017). As PGC-C18 is hydrophobic, it favors the encapsulation of hydrophobic compounds with chloroquine and mefloquine (logP values of 4.63 and 3.9, respectively) encapsulating more effectively than the less hydrophobic sulfadoxine and nitazoxanide (logP of 0.7 and 1.63, respectively) (Fig. 1F). Of the four drugs, mefloquine is the most effectively encapsulated compound with an encapsulation efficiency of $\sim 63\%$. In contrast, sulfadoxine and nitazoxanide lack sufficient encapsulation and exhibit negligible anti-viral activity *in vitro* (Supp. Fig. 2A, B). Therefore, we excluded both compounds from further studies. Likewise, chloroquine displays lower encapsulation efficiency and reduced *in vitro* activity against SARS-CoV-2 in cell models expressing TMPRSS2 compared to MFQ and, thus, we excluded it from further studies as well (Hoffmann et al., 2020; Sacramento et al., 2022). MFQ-loaded PGC-NPs (MFQ-NPs) exhibit controlled release over the span of 5 days in release buffer (i.e., pH 7.4 1X PBS or pH 5.0 Acetate buffer with 1 v/v% Tween 20) with 10-15% of loaded drug released after 48 h and 50-60% release at day 5 (Fig. 1G). MFQ-NPs display a consistent spherical morphology and narrow size distribution (Supp. Fig. 2C, D). Remarkably, MFQ-NPs retain size and dispersity after nebulization, further suggesting that this formulation is suitable for direct drug delivery into the lung (Fig. 1H).

Nanoparticles exhibit minimal *in vitro* cytotoxicity

We evaluated NP cytotoxicity *in vitro* in HFL-1, Vero E6, and Calu-3 cell lines over 24 h via a tetrazolium-based MTS assay (Fig. 2A-C). Vero E6 African Green Monkey kidney epithelial cells and Calu-3 human lung adenocarcinoma cells are widely used models of SARS-CoV-2 infection (Sacramento et al., 2022), whereas HFL-1 cells are human embryonic lung fibroblasts. Unloaded (empty) NPs are relatively non-cytotoxic until dosed at high concentrations (> 1 mg/mL). The IC_{50} values for MFQ-NPs are 42, 54, and 135 $\mu\text{g/mL}$ (corresponding to approximately 7.3, 9.4, and 23.5 μM of loaded MFQ) in HFL1, Calu-3, and Vero E6 cells, respectively. For reference, the IC_{50} values for MFQ in DMSO are 11.3, 12.3, and 16.6 μM for HFL1, Calu-3, and Vero E6 cells, respectively. The vehicle itself (i.e., DMSO) is not cytotoxic at equivalent concentrations without MFQ (Supp. Fig. 2E). Notably, MFQ-NP treatments over 72 h show reduced cytotoxicity compared to the 24 h timepoints in Vero E6 and Calu-3 cells when assessed with the CellTiter Blue assay (Fig. 2D-F). For the 72 h timepoints, MFQ-NP IC_{50} values are 206, and 269 $\mu\text{g/mL}$ (corresponding to approximately 35.8, and 46.8 μM of loaded MFQ) for Calu-3, and Vero E6 cells, respectively. For MFQ in DMSO, the IC_{50} values are 18.8 and 19.6 μM for Calu-3 and Vero E6 cells respectively, using this assay. These data suggest that MFQ-NPs mitigate MFQ cytotoxicity via slowing the release of MFQ into the cytosol compared to the “bolus” kinetics of free drug dosing.

PGC-NPs target the lysosome

To observe NP uptake, we formulated an NP containing covalently linked rhodamine B fluorophore (Rho-NPs) for analysis by flow cytometry and fluorescence microscopy. Flow cytometry reveals a rapid increase in rhodamine fluorescence after as little as 5 min of Rho-NP incubation with Calu-3, Vero E6 and HFL1 cells that steadily increases up to 24 h of Rho-NP incubation (Fig. 3A-B, Supp. Fig. 3A-E).

As flow cytometry by itself is insufficient to demonstrate Rho-NP internalization rather than just surface adsorption, we performed confocal fluorescence microscopy to confirm localization of Rho-NPs in the endo-lysosomal system after cellular uptake (Fig. 3C, D). Indeed, after 1 h of Rho-NP incubation, the majority of Rho-NP fluorescence signal colocalizes with the lysosomal live-cell dye LysoTracker Deep Red (Pearson's coefficient, $r = 0.74$). Rho-NP colocalization with LysoTracker is consistent over a period of 24 h (Fig 3C, D).

MFQ-PGC-NPs inhibit lysosomal activity

Using Vero E6 cells, we evaluated changes in lysosomal pH with the ratiometric probe LysoSensor-Dextran Yellow/Blue. Free MFQ and MFQ-NPs do not increase lysosomal pH but, rather, induce further acidification (Fig. 4A, B). Lysosomal pH of cells treated for 24 h with free MFQ or MFQ-NPs decreases from pH 5.1 to 4.4 ($p < 0.05$). In contrast, treatment for 2 h with 200 nM bafilomycin A1 increases lysosomal pH to 5.7 ($p < 0.01$). Unloaded NPs exert no effect on lysosomal pH. Although MFQ-NPs increase lysosomal acidity, this effect does not correlate with an increase in lysosomal function as free mefloquine and MFQ-NPs promote lysosomal accumulation in Calu-3 and Vero E6 cells (Fig. 4C, D, Supp. Fig. 3F, G). Notably, 24 h treatments with free MFQ and MFQ-NP afford a 2.5-3-fold increase in the amount of lysosomal staining area in Calu-3 cells ($p < 0.001$) and a 6.2-6.9-fold increase in Vero E6 cells ($p < 0.0001$). Bafilomycin A1 treatment strongly inhibits LysoTracker staining presumably by dissipating lysosomal pH. Free MFQ and MFQ-NP treatments, at concentrations above 15 μM , reduce lysosomal protease activity to the same degree as treatment with bafilomycin A1 or the lysosomal protease inhibitors pepstatin A and E64d by 57-75% ($p < 0.01$) (Fig. 4E). Interestingly, MFQ concentrations below 10 μM increase lysosomal protease activity by up to 47% ($p < 0.01$), potentially due to the activation of compensatory lysosomal acidification. Unloaded NPs exhibit no effect on lysosomal protease activity.

MFQ-PGC-NPs inhibit murine coronavirus MHV-A59 infection

Mouse hepatitis virus A59 (MHV-A59) is a beta coronavirus that infects mice displaying neuro-, hepato-, and pneumotropism depending on the route of infection (Cowley and Weiss, 2010). Like SARS-CoV-2, MHV-A59 displays multi-organ involvement and leads to more severe pneumonia in aged individuals (Ryu et al., 2021). L929 mouse fibroblasts infected with MHV-A59-GFP produce a lytic infection with extensive syncytia formation (Supp. Fig. 4A-C). Preliminary studies using L929 cells indicated that MHV-A59-GFP infection, assessed by GFP-positivity, peaked at 20-24 h post infection, after which cell death, measured by Annexin-V-positivity, rapidly sets in (Supp. Fig. 4A, B). Since dying cells rapidly lose their GFP+ signal, we included syncytia formation as an additional measure of viral infection frequency (Supp. Fig. 4C). We adopted a preincubation protocol that allowed us to observe MFQ-NP effects on viral binding and uptake (Fig. 5A). Pre-incubation with empty PGC-NPs exerts no preventive effect on MHV-A59-GFP viral infection

(Fig. 5B, C). In contrast, pre-incubation with MFQ-NPs and free MFQ reduces the amount of GFP+ cells and the incidence of syncytia formation in a dose-dependent manner (Fig. 5B-E) by 29% at 12.5 $\mu\text{g}/\text{mL}$ and up to 97% at the highest concentration of 100 $\mu\text{g}/\text{mL}$ ($p < 0.0001$). At the highest tested concentrations (100 $\mu\text{g}/\text{mL}$ for MFQ-NPs and 10 μM for free MFQ) a slight reduction in overall cell counts occurs compared to infected controls (~20-27% reduction, $p < 0.05$). As a positive control, Remdesivir completely inhibits viral replication at a concentration of 10 μM . Occasionally, individual cells treated with MFQ or MFQ-NPs still exhibit GFP-positive fluorescence; however, the infection did not spread in the culture (Fig. 5B).

MFQ-PGC-NPs inhibit human coronavirus OC43 infection

Like SARS-CoV-2, HCoV-OC43 is a beta coronavirus that causes respiratory tract infections in humans; however, HCoV-OC43 infections are generally mild cold-like symptoms. Vero E6 cells, infected with a high titer of HCoV-OC43 (MOI 1), exhibit pronounced virus positivity after 48 h (Fig. 5F, 'Virus infected Control'). Interestingly, remdesivir treatment results in an incomplete protection against viral infection at 10 μM , reducing viral infection rates by about 69% ($p < 0.05$). Surprisingly, empty NPs inhibit viral infection at the highest tested concentration of 100 $\mu\text{g}/\text{mL}$ with inhibition similar in magnitude to remdesivir controls (68% reduction, $p < 0.05$) (Fig. 5F, G). MFQ-NPs display a concentration dependent inhibition of viral infection that is statistically significant at 50 $\mu\text{g}/\text{mL}$ (70% reduction, $p < 0.05$) (Fig. 5F-I) and reaches almost 100% at 100 $\mu\text{g}/\text{mL}$, whereas free MFQ inhibits viral replication at 10 μM but is only significant at 20 μM , at which concentration one observes substantial cytotoxicity.

MFQ-PGC-NPs inhibit infection with SARS-CoV-2 WT-WA1 and Omicron BA.1 variants

To assess MFQ-NP efficacy against the COVID-19 pandemic virus, SARS-CoV-2, we utilized two different cell lines. Vero E6 cells that do not express human TMPRSS2, therefore favoring SARS-CoV-2 infection by endocytosis, and Calu-3 human alveolar epithelial adenocarcinoma cells with a high expression of TMPRSS2, thus favoring SARS-CoV-2 spike cleavage and fusion at the plasma membrane. We initially adopted a similar pre-infection treatment which did not include washing-off the viral inoculate (Fig. 6A). In Vero cells, remdesivir (10 μM) effectively inhibits SARS-CoV-2 infection (98% reduction, $p < 0.0001$) (Supp. Fig. 5A, B), whereas empty PGC-NPs exhibit no effect, and MFQ-NPs reduce infection only at 100 $\mu\text{g}/\text{mL}$ (79% reduction, $p < 0.0001$). Moreover, free MFQ reduces infection only at 20 μM (93% reduction, $p < 0.0001$) without exhibiting significant toxicity (Supp. Fig. 5A-D). In Calu-3 cells, MFQ-NP treatment at 100 $\mu\text{g}/\text{mL}$ significantly reduces the number of SARS-CoV-2 positive cells (91%, $p < 0.05$) and similarly, strong inhibition was observed by free MFQ at 20 μM (92% reduction, $p < 0.05$) (Fig. 6B-E). In addition to the ancestral SARS-CoV-2 variant, WT-WA1, we assessed MFQ-NP efficacy against Omicron BA.1. After preincubation, empty PGC-NPs exert a small yet significant inhibitory effect on Omicron infection at 25-100 $\mu\text{g}/\text{mL}$ (26-43% reduction, $p < 0.01-0.0001$) (Fig. 6F). MFQ-NPs significantly inhibit Omicron infection at 12.5 and 100 $\mu\text{g}/\text{mL}$ (29% and 83% inhibition, $p < 0.05$ and < 0.0001 respectively) (Fig. 6G). Free MFQ significantly inhibits Omicron infection at 10 and 20 μM (60-97% inhibition, $p < 0.001-0.0001$) (Fig. 6H).

MFQ-PGC-NPs inhibit post-exposure spread of SARS-CoV-2 WT-WA1 and Omicron BA.1

The experimental design used to assess MFQ-NP efficacy under prophylactic treatment conditions cannot distinguish between decreased viral binding and endocytosis, and an inhibition of viral replication. Thus,

to study a potential inhibition of viral replication, we modified the protocol to include a 1 h incubation with SARS-CoV-2 inoculum before starting MFQ-NP treatments, which allows for viral attachment and uptake prior to the beginning of the treatment (Fig. 6I). Unloaded-PGC-NPs do not prevent SARS-CoV-2 WT-WA1 replication but exhibit a significant effect in Omicron infected Calu-3 cells (49% reduction, $p < 0.05$) (Fig. 6J, M). MFQ-NPs inhibit viral replication of the ancestral WT-WA1 variant to a non-significant degree (77% reduction, $p = 0.11$) and significantly reduce Omicron replication at 50 and 100 $\mu\text{g}/\text{mL}$ (56% and 84% reduction, $p < 0.01$ and < 0.001) (Fig. 6K, N), which is similar to the result obtained with free MFQ at 10 and 20 μM (up to 98% reduction of Omicron positive cells, $p < 0.0001$) (Fig. 6L, O). These data suggest that MFQ-NPs inhibit viral uptake as well as replication.

DISCUSSION

COVID-19 highlights the capacity of a sudden infectious disease to cause a long-lasting impact on public health. In response to the emergence of SARS-CoV-2, scientists rapidly developed prophylactic vaccines and began repurposing already available drugs to treat hospitalized patients. In this study we focused on developing nanoparticles (NPs) using a biocompatible polymer we have developed, poly(glycerol monostearate-co- ϵ -caprolactone) (PGC-C18), for the effective pulmonary delivery of antiviral drugs, particularly for the treatment of coronavirus infection. PGC-C18 was selected due to our experience with this polymer in a different drug delivery form factor (i.e., an implantable surgical mesh), its successful completion of 10993 biocompatibility testing required by the FDA (Kaplan et al., 2016), and its availability via large-scale GMP production processes that would speed translation to the clinic. Furthermore, PGC-C18 exhibits superior long-term compound release properties and lacks an initial drug “burst” release associated with unmodified or short chain fatty acid modified PGC surfaces (Wolinsky et al., 2010, 2012).

Other groups have similarly leveraged polymer systems to physically encapsulate antibiotics or antimicrobials for pulmonary delivery (Al-Halifa et al., 2019; Coowanitwong et al., 2008; Ungaro et al., 2012). Polylactic acid (PLA) and poly(lactic-co-glycolic acid) (PLGA) are commonly employed as they are biodegradable and biocompatible polymers already approved by the Food and Drug Administration (FDA) and European Medicines Agency (EMA) for use in humans. However, these formulations tend to form particles ≥ 200 nm with many manufacturing approaches resulting in microspheres on the μm -size scale. Multiple particle deposition studies suggest that NPs > 100 nm fail to reach deep lung tissue (i.e., the alveoli), which makes these polymer platforms a less attractive approach for prophylactics/treatments against coronaviruses, such as SARS-CoV-2, as this virus largely targets alveolar type 2 (AT2) cells, one of the major cell types that co-express ACE2 and TMPRSS2 (Geiser and Kreyling, 2010; Liu et al., 2021; Löndahl et al., 2014)

We fabricated PGC-NPs using an emulsification and solvent evaporation method which yielded NPs between 100-150 nm in diameter with low polydispersity (< 0.17) and low vehicle cytotoxicity. These NPs physically encapsulated small molecule drugs, and the encapsulation efficiency increased with increasing hydrophobicity/lipophilicity (i.e., logP) of the drugs. The NPs were loaded with chloroquine, mefloquine, sulfadoxine, and nitazoxanide. Among the drugs, mefloquine was found to be the most effectively encapsulated compound with an encapsulation efficiency of $\sim 63\%$. MFQ-loaded NPs exhibited controlled release and retained their size and dispersity after nebulization, making them suitable for direct drug

delivery into the lung. Furthermore, the NPs exhibited minimal *in vitro* cytotoxicity in human lung fibroblast (HFL-1), Vero E6, and Calu-3 cell lines, making them suitable for clinical translation.

Of the investigated drugs, mefloquine shows improved activity against SARS-CoV-2 over other repurposed drug candidates such as hydroxychloroquine and chloroquine yet remains under-investigated as an antiviral therapy (Sacramento et al., 2022; Shionoya et al., 2021). Jan *et al.* report that orally administered treatment of MFQ at 30 mg/kg/day for 3 days results in the absence of weight loss in SARS-CoV-2 infected hamsters (Jan et al., 2021). However, viral lung titers only decrease by less than one log unit and no further investigation regarding disease progression or lung histology was reported. Preliminary pharmacokinetic modeling suggests that conventional (i.e., oral) dosing of MFQ requires multiple high doses (e.g., 350 – 450 mg) daily to achieve therapeutic plasma concentration, likely impeding clinical translation of orally-dosed MFQ. Alternatively, pulmonary delivery of MFQ would enable higher concentrations in lung tissue, reduce systemic exposure and mitigate off-target toxicities (i.e., neurotoxicity), while eliminating the need for repeat daily doses. As a first step towards this goal, we designed a polymer-based nanoparticle to deliver mefloquine locally to the respiratory tract, the site of SARS-CoV-2 infection. MFQ-NPs exhibited robust and dose-dependent viral inhibition across multiple coronavirus strains including MHV, HCoV-OC43, and SARS-CoV-2 (USA-WA1/2020 and Omicron BA.1 variants). Additionally, unlike hydroxychloroquine and chloroquine, MFQ is efficacious against SARS-CoV-2 infection in cell lines expressing both ACE2 and TMPRSS2 (e.g., Calu-3) (Fig. 6 and (Sacramento et al., 2022; Shionoya et al., 2021)).

Despite mefloquine being used as an antimalarial drug similar to chloroquine, little is known about the biological response to mefloquine treatment, particularly regarding lysosomal acidification. In acute myeloid leukemia cells, mefloquine disrupts lysosomal integrity while exerting a biphasic effect on lysosomal pH (Sukhai et al., 2012; Lam Yi et al., 2019). Herein, we observed that treatment with mefloquine or MFQ-NPs decreases lysosomal pH with a concomitant increase in lysotracker accumulation when compared to non-treated controls. Interestingly, further acidification as a result of mefloquine treatment corresponds to an inhibition of proteolytic degradation at high dosages. Unlike chloroquine, which is a known lysosomotropic agent that increases lysosomal pH, leading to a decrease in lysosomal proteolytic activity, mefloquine inhibits proteolytic activity while exerting the opposite effect on lysosomal pH at therapeutic dosing (Hoffmann et al., 2020). At sub-therapeutic dosing in our study, mefloquine treatment decreased lysosomal pH and increased proteolysis but, conversely, lysosomal accumulation increased over baseline. These effects on lysosomal pH and activity resemble a biphasic dose response (hormesis) described previously for chloroquine and its derivatives and may explain the varied outcomes in the treatment of COVID-19 patients with lysosomotropic drugs (Calabrese et al., 2021; Moore, 2020).

Proposed mechanisms for the antiviral effect of mefloquine against coronaviruses and other viruses such as Ebola and monkeypox virus include the inhibition of viral uptake by endocytosis and plasma membrane fusion and release of the viral genome from endosomes; however, a molecular basis for the mechanism is not reported (Akazawa et al., 2023; Sacramento et al., 2022; Shionoya et al., 2021). In fact, MFQ's effect on endocytosis has not been studied extensively in mammalian cells. In the malaria parasite *Plasmodium falciparum*, mefloquine inhibits the endocytosis of hemoglobin from host-erythrocytes without affecting

endosome-vacuolar fusion in the parasite suggesting a specific inhibitory effect on the formation of endocytic vesicles (Hoppe et al., 2004). Interestingly, even at a dosing of 20 μ M mefloquine, we observed individual cells stained positive for viral proteins, suggesting that these cells internalized and replicated viral genomes (see Fig. 5B, F; Fig. 6B; Supp. Fig 4A). However, the surrounding cells did not stain positive even after being in contact with infected cells for periods of time that correspond to multiple SARS-CoV-2 replication cycles. The release/escape of coronaviruses, including SARS-CoV-2, from the cell predominantly relies on exocytosis rather than cell lysis in the first 48 h of infection (Calabrese et al., 2021; Cortese et al., 2020). To that end, coronaviruses hijack autophagic vesicles rather than exocytic vesicles for release (Chen et al., 2021; Miller et al., 2020; Münz, 2017). Mefloquine does not inhibit canonical exocytosis but is a potent inhibitor of autophagic vesicle turn-over by inhibiting lysosomal proteases such as cathepsin B (Balasubramanian et al., 2017; Chen et al., 2021; Golden et al., 2015; Sharma et al., 2012). We also observed an inhibition of lysosomal protease activity in our study. This effect varies across cell lines in the literature and was conversely interpreted in some studies as autophagy induction at concentrations that could induce a hormetic compensation (Shin et al., 2015; Xie et al., 2020). We therefore suggest that mefloquine inhibits viral release by blocking both autophagy and viral uptake.

To date, no aerosolized treatment is currently approved against coronaviruses, though local delivery to the lung to treat respiratory viruses is a logical treatment approach (He et al., 2022). Indeed, several groups are exploring aerosolized treatments for COVID-19, with particular interest in developing Remdesivir containing formulations (Ramsey et al., 2022; Vartak et al., 2021). However, similar to nirmatrelvir and molnupiravir, passage of SARS-CoV-2 WT-WA1 in the presence of remdesivir results in resistance mutations in the RNA dependent RNA polymerase (RdRp) that confer resistance (i.e., 2.7-to 10.4-fold shift in EC_{50}) to RDV antiviral activity (Stevens et al., 2022). NPs loaded with mefloquine (MFQ-NPs) exhibit a robust inhibition of coronavirus infection *in vitro* across multiple viral strains (i.e., MHV-A59, HCoV-OC43, and SARS-CoV-2 WT-WA1 and Omicron BA.1) in cells that model the human pulmonary epithelium (i.e., Calu-3). In summary, we describe a new polymeric nanoparticle system, composed of PGC-C18, which physically encapsulates hydrophobic small molecules with antiviral properties. These results encourage further *in vivo* investigation and development of MFQ-NPs for use as either a prophylactic or treatment for an array of respiratory coronaviruses.

LIMITATIONS OF THE STUDY

Several limitations are present in the current study. First, the *in vitro* effective mefloquine concentration of ca. 17.4 μ M required in our viral inhibition assays is slightly higher than in other comparable studies (Sacramento et al., 2022; Shionoya et al., 2021). This result may be a consequence of using 10-100x higher viral MOIs than comparable studies. That said, our MFQ-NPs do not release their entire drug payload in an immediate burst but rather slowly over time and exhibit low cytotoxicity and a potent antiviral effect even under a high viral burden. Our study shows that MFQ loaded NPs are an effective treatment against SARS-CoV-2 infection. More investigation is needed to determine whether MFQ-NPs release sufficient MFQ in animal lung tissues and if MFQ-NP treatment is effective in preventing or mitigating SARS-CoV-2 infection *in vivo*.

METHODS

Chemicals

Sodium dodecyl sulfate (L4509), chloroquine diphosphate (C6628) and mefloquine hydrochloride (M2319) were purchased from Sigma-Aldrich (St. Louis, MO). Sulfadoxine (S0899) and nitazoxanide (N1031) were purchased from TCI Chemicals (Tokyo, JP). DQ Red BSA reagent (D12051), LysoTracker Deep Red (L12492), LysoTracker Green DND-26 (L7526), and LysoSensor Yellow/Blue dextran (L22460) were purchased from Invitrogen (Waltham, MA). CellTiter 96 AQueous One Solution Cell Proliferation Assay (MTS) and CellTiter Blue were purchased from Promega (Madison, WI). Annexin V-Orange (4759) was purchased from Sartorius (Göttingen, DE)

Antibodies used in this study were against the nucleoprotein of HCoV-OC43, clone 542-7D (MAB9013, Sigma-Aldrich) and against the SARS nucleocapsid protein (200-401-A50, Rockland Immunochemicals Inc, Limerick, PA).

Free base chloroquine was prepared from the phosphate salt following previously published procedures (Dodd and Bohle, 2014). Briefly, chloroquine diphosphate salt was dissolved in water in a separatory funnel and sodium hydroxide (1 M) was added until all drug precipitated. The precipitate, free base chloroquine, was extracted with dichloromethane, dried over sodium sulfate, filtered, and dried under vacuum overnight.

Synthesis of PGC-C18 and PGC-C18-Rho

Poly(1,3-glycerol monostearate-co- ϵ -caprolactone) (PGC-C18) was synthesized following previously published procedures (Wolinsky et al., 2007; Wolinsky et al., 2012). Briefly, ϵ -caprolactone and 5-benzyloxy-1,3-dioxan-2-one monomers were combined in a Schlenk flask at a molar ratio of 4:1, respectively. This flask was then evacuated and flushed three times with N₂. The flask was then partially submerged in an oil bath and heated to 140°C. Separately, the tin catalyst (Sn(Oct)₂, molar ratio of monomer: initiator = 500:1) was added to a separate flask and dried under vacuum for 1 h. Dry toluene was added to the catalyst and the toluene/catalyst mixture was then injected via syringe into the monomer containing flask. The reaction was stirred at 140°C for 48 hours until the solution became viscous. The reaction was then removed from heat, and the polymer was dissolved in dichloromethane (DCM) and precipitated in cold methanol three times. The solvent was decanted, and the resulting polymer, poly(5-benzyloxy-1,3-dioxan-2-one-co- ϵ -caprolactone) (PGC-Bn), was dried under vacuum overnight and isolated as a white solid.

The benzyl-protecting groups were then removed via palladium-catalyzed hydrogenolysis. The resulting mixture was filtered through Celite to remove the palladium on carbon (Pd/C), yielding poly(glycerol-co- ϵ -caprolactone), or PGC-OH. Poly(glycerol-co- ϵ -caprolactone) (1 mol eq.), stearic acid (0.3 mol eq.), dicyclohexylcarbodiimide (0.24 mol eq.), and 4-dimethylaminopyridine (0.1 mol eq.) were dissolved in dichloromethane and stirred at room temperature for 18 h. The dicyclohexylurea was removed via filtration and the product, poly(1,3-glycerol monostearate-co- ϵ -caprolactone) (PGC-C18), was dissolved in dichloromethane (DCM) and precipitated in cold methanol three times. The solvent was decanted, and the final product, PGC-C18, was dried under vacuum overnight. Monomer and polymer structure were characterized by proton (¹H) nuclear magnetic resonance spectroscopy (NMR) using a Varian INOVA 500

MHz instrument at the Boston University Chemical Instrumentation Center (BU-CIC). All spectra were obtained at ambient temperature with compounds dissolved in CDCl₃ (7.25 ppm for ¹H NMR) (Supp. Fig 1A,B). PGC-C18 polymer molecular weight and dispersity were determined against polystyrene standards using an Agilent 1260 Infinity II GPC-SEC equipped with refractive index and dual-angle light scattering detectors (Supp. Fig 1C).

For fluorescent polymer, poly(glycerol-co- ϵ -caprolactone) (1 mol eq.), rhodamine B (0.2 mol eq.), dicyclohexylcarbodiimide (0.22 mol eq.), and 4-dimethylaminopyridine (0.1 mol eq.) were dissolved in dichloromethane and stirred at room temperature for 18 h. Next, stearic acid (0.8 mol eq.) was added and stirred at room temperature for an additional 18 h. Lastly, the dicyclohexylurea was removed via filtration and the product, poly(glycerol monostearate-co- ϵ -caprolactone) rhodamine B (PGC-C18-Rho), was dissolved in dichloromethane (DCM) and precipitated in cold methanol three times. The solvent was decanted, and the final product, PGC-C18-Rho, was dried under vacuum overnight.

Preparation of PGC-NPs

PGC-NPs were fabricated similarly to a previously described solvent evaporation approach (Ekladius et al., 2017). The core components, PGC-C18 (200 mg) and free drug (mefloquine, sulfadoxine, chloroquine, nitazoxanide – 25 mg, 12.5 wt%) are dissolved in 2 mL dichloromethane. This solution was placed in a sonication bath for 5 min to quickly form a homogenous solution. The surfactant, sodium dodecyl sulfate (SDS, 80 mg) is separately solubilized in 10 mM pH 7.4 phosphate buffer (8 mL). These two solutions were then added via syringe into a sonochemical reaction vessel and emulsified under an argon blanket in a pulsatile manner (30min total, 1s on / 2s off) using a Sonics Vibra-Cell VCX-600 Ultrasonic Processor (Sonics & Materials; Newtown, CT). The resulting nano-emulsion is transferred to a clean glass vial under magnetic stirring for at least 1 h to allow the dichloromethane to evaporate from the NP solution. To ensure the elimination of unassociated SDS, the nano-emulsion is then dialyzed for 24 hours against 2 L of 5 mM pH 7.4 phosphate buffer using SnakeSkin dialysis tubing (MWCO 10Kda).

Rho-NPs were fabricated similarly, with core consisting mainly of PGC-C18 (140 mg) with a small portion of fluorescent polymer, PGC-C18-Rho (60 mg). By primarily using the traditional PGC-C18 polymer, nanoparticle structure and size remains unperturbed, yet the particles fluoresce and are visible via microscopy and flow cytometry.

Scanning electron microscopy

Unloaded NPs and MFQ-NPs were diluted 1:100 – 1:1000 times in nanopure water. Aliquots were pipetted onto silicon wafers affixed to aluminum stubs with copper tape and allowed to air dry overnight. The stubs were then sputter coated with 5 nm Au/Pd. Samples were then imaged using a Supra 55VP field emission scanning electron microscope (Carl Zeiss AG, Jena, Germany) with an accelerating voltage of 3-5 kV and working distance of 6 mm.

Dynamic light scattering

For sizing measurements, 75 μL of NP solution is diluted in 3 mL nanopure water, and for zeta potential measurements, 30 μL of NP solution is diluted in 1.5 mL 1X phosphate buffered saline (PBS). Samples are pipetted into a cuvette and size and zeta potential are then obtained using the Brookhaven NanoBrook Omni (Brookhaven Instruments; Holtsville, NY). All measurements were performed in triplicate ($n = 3$).

Quantification of drug loading and release

Small molecule drug loading (e.g., mefloquine, chloroquine, nitazoxanide, sulfadoxine) was measured using high performance liquid chromatography (HPLC). Serial dilution standards were prepared in a mobile phase composed of: 45% - 0.1% triethylamine / phosphate buffer (pH 3.0) and 55% - acetonitrile. Standard samples for each pharmacologic agent were run for 8 min through a Zorbax SB300 - C18 column (150 mm length) and detected through UV absorbance to generate a standard curve. To quantify NP loading, NPs were disrupted by adding acetonitrile to a final volume of 90% (v/v). This solution was then re-equilibrated by adding aqueous buffer to match mobile phase composition. This solution was filtered through a 0.22 μm PVDF syringe filter (Millipore) to remove large aggregates or dust prior to running samples. Samples were run similar to standards.

Mefloquine drug release from MFQ-NPs was measured using UPLC-MS (Waters ACQUITY; Milford, MA). Briefly, undiluted MFQ-NPs were loaded into Slide-A-Lyzer™ MINI Dialysis Devices, 10K MWCO (PI88401), and placed into 14 mL of release buffer (either 1X PBS (pH 7.4) with 1 v/v% Tween 20 or 0.1 M Acetate buffer (pH 5.0) with 1 v/v% Tween 20) in a conical tube. Samples were placed in a 37°C oven equipped with a shaker plate, and MFQ release was measured from the release buffer at 4, 24, 48, 72, 96, and 120 h timepoints. UPLC-MS samples were run on a Waters Acquity UPLC with a binary solvent manager, SQ mass spectrometer, Waters 2996 PDA (photodiode array) detector, and evaporative light scattering detector (ELSD) using an Acquity UPLC BEH C18 1.7 μm , 2.1 x 50 mm column (186002350). Serial dilution standards were prepared in a mobile phase composed of: 50% - release buffer (i.e., 1X PBS (pH 7.4) or 0.1 M Acetate buffer (pH 5.0)) and 50% - acetonitrile.

qNano

Particle size and size distribution was also measured using a qNano analyzer (IZON Sciences) coupled with an adjustable nanopore (NP150), and air based variable pressure module (VPM). MFQ-PGC-NPs and carboxylated polystyrene calibration particles (CPC100, IZON Sciences) were diluted 1:500 – 1:1000 times in tris buffer electrolyte (IZON Sciences) prior to running samples according to manufacturer's protocol. Each recorded measurement consisted of at least 500 particles counted in a 5–10 min duration. Particle size and distribution was measured using Izon control suite software.

Nebulization

MFQ-NPs were first fabricated as described and diluted to respective concentrations using 10mM pH 7.4 phosphate buffer to prevent clogging of the vibrating meshes in the nebulizer at high concentrations. Diluted NPs were pipetted into the top reservoir of an Aerogen® Pro nebulizer and a conical tube was used to collect nebulized vapor. Centrifugation was used to condense the vapor into a liquid solution.

Nebulized MFQ-NPs were compared to the pre-diluted sample as well as pre-nebulized dilutions for size and morphological changes using DLS and SEM as described.

Cell culture

Vero E6 cells were obtained from the American Type Culture Collection (CRL-1586, ATCC, Manassas, Virginia) and grown in Eagle's Minimal Essential Medium (Corning, Corning, NY) supplemented with 10% FBS and Penicillin (100 U/mL)/Streptomycin (100 µg/mL) (PenStrep, Gibco, Waltham, MA). Calu-3 human lung cancer cells were obtained from ATCC (HTB-55) and grown in EMEM supplemented with 10% FBS and PenStrep. L929 and 17CL-1 mouse fibroblast cells were a kind gift from Volker Thiel's lab at the University of Bern and Elke Mühlberger's lab at Boston University and grown in EMEM supplemented with 10% FBS and Primocin (100 µg/ml) (Invivogen, San Diego, CA). HCT-8 cells were obtained from ATCC (CCL-244) and grown in RPMI-1640 (ATCC) supplemented with 10% horse serum. HFL1 cells were obtained from ATCC (CCL-153) and grown in F-12K media supplemented with 10% FBS and PenStrep.

Viruses

SARS-CoV-2 USA-WA1/2020 (referred to as WT-WA1) and Omicron BA.1 were obtained from the Biodefense and Emerging Infections (BEI) Resources of the National Institute of Health (contributed by Mehul Suthar). All work with SARS-CoV-2 was performed at the UCLA high containment laboratory at biosafety level 3. SARS-CoV-2 was propagated and passaged in Vero E6 cells. HCoV-OC43 was obtained from ATCC (VR-1558) and propagated in HCT-8 cells. MHV-GFP was a kind gift from Volker Thiel's lab at the University of Bern and Elke Mühlberger's lab at Boston University. MHV-A59-GFP was propagated in 17CL-1 cells. Viral titers were determined by assessing viral cytopathic effect (CPE) by microscopy in cells infected with serial 10-fold dilutions respectively. TCID₅₀/ml was calculated using the Reed-Muench method.

***In vitro* cell viability**

The cytotoxicity of NPs with and without MFQ was evaluated using a tetrazolium-based MTS cell proliferation assay (Promega CellTiter 96 Aqueous One Solution Cell Proliferation Assay). HFL1, Calu-3, and Vero E6 were cultured in a 96-well plate at 12000 cells/well for 1 day, after which the media was exchanged for media containing no treatment or unloaded PGC-NPs (1.95, 3.91, 7.81, 15.63, 31.25, 62.5, 125, 250, 500, 1000 µg/mL NPs) or MFQ-NPs (1.95, 3.91, 7.81, 15.63, 31.25, 62.5, 125, 250, 500, 1000 µg/mL NPs) or free MFQ solubilized in DMSO (0.78, 1.56, 3.13, 6.25, 12.5, 25, 50 µM) or DMSO as a vehicle control (0.031, 0.063, 0.125 % v/v relative to culture media). The cells were then incubated with treatment for 24 hours, after which cell viability was quantified with a SpectraMax iD3 (Molecular Devices) plate reader relative to the no treatment control, after correcting for background absorbance. Alternatively, toxicity was determined using the CellTiter Blue assay (Promega). Vero E6, or Calu-3 cells were seeded in clear 96-well plates and treated with MFQ-NPs at 1 µg/mL – 800µg/mL, unloaded NPs, or equivalent concentrations of free MFQ solubilized in dimethyl sulfoxide (DMSO) for 72 h. Subsequently, CellTiter reagent was added to the wells for 1 h and fluorescence emission was measured at ex:565 nm, em:620 nm using a Tecan Spark 10M plate reader (Tecan Ltd., Männedorf, Switzerland).

Cellular uptake of Rho-PGC-NPs via flow cytometry

FACS analysis of Rho-NPs treated cells was performed with an Attune NxT Flow Cytometer (Invitrogen). HFL1, Calu-3, and Vero E6 were cultured in a 96-well plate at 12000 cells/well for 1 day, after which the media was exchanged for media containing 75 µg/mL Rho-NPs. The cells were then incubated with treatment for 24 hours, after which cells were trypsinized, washed with PBS by centrifugation, resuspended in FACS buffer (PBS + 2% FBS) and then subjected to flow cytometry. Cell debris was excluded by gating on the forward and side scatter plot. Intensity bar graph for uptake is displayed as mean values calculated from median fluorescence intensity for cell population identified as positive based on the gating strategy.

Cellular localization of Rho-PGC-NPs via confocal microscopy

HFL1 were grown on 12-well glass bottom plates (Celvis, P12-1.5H-N) at a density of 50000 cells/well and grown for 24 h. Cells were then treated with a 75 µg/mL dose of Rho-NPs for 1 h, 4 h, or 24 h. Cells were then washed with 1X PBS and incubated with 50 nM LysoTracker Deep Red (Invitrogen) in culture media for 1.5 h. Following acidic organelle labelling, cells were washed with PBS and incubated with 1 µg/mL Hoechst 33342 (Thermo) and 5 µg/mL Wheat Germ Agglutinin Oregon Green 488 Conjugate (Invitrogen) for 10 min at 37 °C. Cells were then washed with 1X PBS and incubated with 1 µg/mL Hoechst 33342 in Live Cell Imaging Solution (Thermo) and imaged immediately on an Olympus FV3000 confocal microscope with a temperature control chamber at 37 °C. Cells were imaged using a 60X oil immersion objective. Co-localization of Rho-NPs and LysoTracker dye was determined by calculating Pearson's coefficient using CellProfiler (Carpenter et al., 2006).

Lysosensor-Dextran Yellow/Blue imaging

Vero E6 cells were seeded at a density of 10,000 cells/well into Greiner CellView 4 compartment dishes. After 24 h cells were stained with 5 mg/mL Lysosensor-Dextran Yellow/Blue dye in EMEM for 3 h following an overnight media chase. The next day cells were incubated for 24 h with 100 µg/mL NPs (±MFQ) or 10 or 20 µM MFQ. Bafilomycin A1 was added at a concentration of 200 nM as alkalization agent 2-4 h before imaging. Imaging was performed using a Zeiss LSM880 (Carl Zeiss AG, Jena, Germany) equipped with a Coherent 2-photon laser at a 2-photon excitation of 720 nm and 2 emission bands at 400-480 nm (blue) and 510-620 nm (yellow) using a 63X oil immersion objective. pH standard curves were generated by permeabilizing Lysosensor-Dextran Yellow/Blue stained cells with 10 µM nigericin, 20 µM monensin in pH clamped buffers ranging from pH 4.5 – 6.0. Lysosomal ROIs and Yellow/Blue staining intensity were determined using CellProfiler.

Lysotracker Green Imaging

Vero E6 cells were seeded at a density of 10,000 cells/well into 96-well Greiner µClear imaging plates. After 24 h cells were treated with 50-100 µg/mL NPs (±MFQ), 20 µM MFQ, or 200 nM bafilomycin A1 for 24 h and subsequently stained with 1 µM LysoTracker Green and Hoechst 33342. Cells were imaged using an Operetta High-Content Imager (PerkinElmer Inc, Waltham, MA) using a 20X air objective and lysosomal

accumulation defined as LysoTracker positive signal area % in expanded nuclear ROIs. Images were analyzed using CellProfiler.

DQ-Red BSA Assay

HFL1 cells were cultured in a 96-well plate at 15000 cells/well for 24 h, after which the media was exchanged for media containing no treatment, empty NPs (12.5, 25, 50, 75, 100 µg/mL NPs) or MFQ-NPs (12.5, 25, 50, 75, 100 µg/mL NPs) for 24 h. Control treatments include Bafilomycin A1 (200 nM), and Pepstatin A (10 µg/mL) + E64d (10 µg/mL) for 4 h, or free MFQ (10, 15 µM) for 24 h. Following treatment, cells were washed with 1X PBS and incubated with 10 µg/mL DQ Red BSA reagent (Thermo) in culture media for 1 h. After incubation with assay reagent, cells were trypsinized, washed with 1X PBS by centrifugation, resuspended in FACS buffer (PBS + 2% FBS) and then subjected to flow cytometry. Cell debris was excluded by gating on the forward and side scatter plot. Relative protease activity is displayed as mean values calculated from median fluorescence intensity for cell population identified as positive based on the gating strategy.

MHV-GFP infection kinetics determination

In order to determine the best timepoint to assess MHV-A49 (MHV-GFP) infection. L929 cells were seeded in clear bottom Corning 96-well plates and inoculated with MHV-GFP at an MOI of 0.1. A 1:500 dilution of Annexin V-Orange (Sartorius) was added to the cells to monitor MHV induced cell lysis and cell death. Cells were imaged every hour for 48 h using an OmniFL live cell analysis platform (CytoSMART Technologies, Eindhoven, NL) and growth curves were determined using Cytosmart cloud software.

NP treatments and viral infections

For MHV-A49 infection and HCoV-OC43 assays L929 or Vero E6 cells are plated into 96-well Corning imaging plates. 24 h later, cells undergo a 1 h prophylactic pre-treatment with NPs ± MFQ (12.5-100 µg/mL), free MFQ (1.25-20 µM), positive control treatment (10 µM remdesivir), or no treatment. Following pre-treatment, media is replaced with serum free media containing virus (HCoV-OC43 at MOI of 1 or MHV at MOI of 0.1) for 1 h. After 1 h of inoculation, viral containing media is removed, wells are rinsed with 1X PBS and treatments are added back to the wells for another 24-48 hrs. Cells are then fixed with 4% paraformaldehyde, permeabilized with 0.1% Triton X-100 in PBS, blocked with 2% BSA, 5% normal donkey serum (NDS), and infection is visualized by immunofluorescence staining of pan-corona-nucleocapsid protein for HCoV-OC43 with a mouse monoclonal primary and a donkey-anti-mouse AlexaFluor488 conjugated secondary antibody and cell nuclei counterstaining with DAPI. MHV-GFP positive cells will appear GFP-fluorescence positive or as syncytia.

For SARS-CoV-2 infection assays, Vero E6 or Calu-3 cells were plated into 96-well, clear-bottom imaging plates. 24 h later, cells undergo a 1 h prophylactic pre-treatment in 100 µL of media containing 2X concentrated NPs ± MFQ (25-200 µg/mL), free MFQ (2.5-40 µM), positive control treatment (20 µM remdesivir), or no treatment. Following pre-treatment, 100 µL of media containing virus (SARS-CoV-2 at MOI of 0.1 for Vero E6 and MOI of 0.2 for Calu-3 cells) is added to the wells diluting the treatments to 1X for another 48 h. Alternatively, for post-inoculation treatments, Calu-3 cells are infected with SARS-CoV-

2 MOI 0.2 diluted in serum free EMEM for 1 h. Subsequently, the inoculum is removed, the cells washed once with DPBS, and treated with NPs \pm MFQ (12.5-100 $\mu\text{g}/\text{mL}$), free MFQ (1.25-20 μM), positive control treatment (10 μM remdesivir), or no treatment for 48 h. Cells are then fixed with 4% paraformaldehyde, permeabilized with 0.1% Triton X-100 in PBS, blocked with 2% BSA, 5% NDS, and infection is visualized by immunofluorescence staining of SARS-CoV-2 N protein with a rabbit polyclonal primary and a donkey-anti-rabbit AlexaFluor568 conjugated secondary antibody and cell nuclei counterstaining with DAPI. Plates were imaged with an Operetta High-Content imager using a 10X air objective, and images were processed using CellProfiler. Positive cells were determined as expanded nucleus ROIs containing above threshold virus positive staining, syncytia were defined as irregularly close nucleus clusters of $>40 \mu\text{m}$ diameter.

Statistical analysis

Unless otherwise noted, all experiments were repeated at least three times. Unless otherwise mentioned data were graphed and analyzed using GraphPad Prism 9.1. Data are displayed as means \pm SD or SEM where appropriate. To determine statistically significant differences one-way and two-way ANOVA analysis with Dunnet post-hoc tests were applied where appropriate.

ACKNOWLEDGEMENTS

The authors would like to thank Drs. Stan Louie and Daniel Dagan for valuable discussion and critical reading of the manuscript. We would also like to thank the team at Aerogen (Patricia Dailey, Ronan MacLoughlin, and David Coyle) for gifting multiple Aerogen[®] Solos and controllers for nebulization. In addition, we would like to thank Dr. David Ferrick and the team at Axion Biosystems for the kind gift of the CytoSMART OmniFL. This project was supported by UCLA COVID-19 Emergency Response OCRC Grant #20-21 to Orian Shirihai. B.M.T. and A.M. were funded through the BUnano Fellowship Program.

AUTHOR CONTRIBUTIONS

Conceptualization: A.P., B.M.T., A.H.C., M.W.G., and O.S.S

Methodology: A.P., B.M.T., and V.A.

Advice: V.A.

Investigation: A.P., B.M.T., A.M., S.A., A.J.B, R.A.S, B.S., G.G. Jr., and M.V.

Visualization: A.P., B.M.T., A.M., S.A.

Supervision: A.H.C., M.W. G., and O.S.S

Writing—original draft: A.P., B.M.T.

Writing—review & editing: All authors

Funding: B.M.T., A.M., M.W. G., and O.S.S

Conflict of interest

B.M.T., A.P., A.H.C., O.S., and M.W.G. are co-inventors on a patent application, which is available for licensing (PCT/US22/45913). All other authors declare they have no competing interests.

Data Availability

The raw data required to reproduce these findings are available from the authors upon request.

ORCID and EMAILS

Name	Email	ORCID
Brett M. Tingley	btingley@bu.edu	0000-0001-8980-8679
Anton Petcherski	apetcherski@mednet.ucla.edu	0000-0002-3143-3867
Andrew Martin	ajmart@bu.edu	0000-0002-7512-5049
Sarah Adams	scadams@bu.edu	0000-0002-9527-8157
Alexandra J. Brownstein	brownsa@g.ucla.edu	0000-0003-0920-722X
Ross A. Steinberg	rossasteinberg@gmail.com	0000-0002-3530-2557
Byourak Shabane	Byourak.shabane@gmail.com	0000-0001-9249-5917
Gustavo Garcia Jr.	gustavogarcia@mednet.ucla.edu	0000-0002-1649-9251
Michaela Veliova	mveliova@gmail.com	0000-0003-1117-691X
Vaithilingaraja Arumugaswami	varumugaswami@mednet.ucla.edu	0000-0002-6872-5118
Aaron H. Colby	acolby@bu.edu	0000-0001-7161-821X
Orian S. Shirihai	oshirihai@mednet.ucla.edu	0000-0001-8466-3431
Mark W. Grinstaff	mgrin@bu.edu	0000-0002-5453-3668

FIGURE LEGENDS

Figure 1. Formulation of novel PGC-C18 nanoparticles. (A) Chemical structure of poly(1,3-glycerol monostearate-co- ϵ -caprolactone) (PGC-C18). (B) Schematic structure of PGC nanoparticle containing sodium dodecyl sulfate surfactant and antiviral drug payload. (C) Electron micrographs of unloaded PGC-NPs demonstrate sizes around 100 nm and round morphology. Scale Bar=200 nm. (D) NP size and polydispersity measurements using dynamic light scattering (DLS) confirm nanoparticle sizes around 100-150 nm for unloaded and small molecule loaded NPs. (E) Charge measurement of NPs using DLS. (F) Encapsulation efficiency of drug compounds in NPs as measured by high performance liquid chromatography (HPLC). Drug loading concentrations are graphed as colored bars and measured on the left y-axis. Compound encapsulation efficiencies are graphed as dots (●) and measured on the right y-axis. (G) Mefloquine release from mefloquine loaded NPs (MFQ-NPs) over 5 days in pH 7.4 and pH 5.0 release buffer. Release is plotted as a % of drug released relative to initial drug loading at day 0. (H) Size and polydispersity measurements by DLS confirm nanoparticle stability after nebulization with Aerogen® Solo. All experiments in A-G represent n=3-5 NP batches. All data are displayed as means \pm SD.

Figure 2. Cytotoxicity of PGC-C18 nanoparticles. Cell viability measurements by MTS assay in HFL1, Calu-3, or Vero E6 cells treated with (A) unloaded PGC-NPs, (B) Mefloquine loaded NPs (MFQ-NPs), (C) free molecular MFQ for 24 h or by CellTiter Blue assay in Calu-3 or Vero E6 cells treated with (D) unloaded PGC-

NPs, (E) MFQ-NPs, (F) free MFQ for 72 h. All data are displayed as means \pm SEM. All experiments represent n=3-6.

Figure 3. Nanoparticle uptake and localization. Rho-NP uptake measured by flow cytometry in Calu-3 cells and displayed as (A) representative intensity histogram or (B) median intensity bar graph. (C) Confocal microscopy imaging of Rho-NPs and lysosomes labelled with LysoTracker Deep Red in HFL1 cells after 1 h, 2 h, 4 h, and 24 h of NP incubation demonstrates very high levels of colocalization (quantified as Pearson's *r* coefficient in (D)). Scale bars=10 μ m; zoom-in box scale bars=2 μ m. Flow cytometry experiments represent n=6; imaging experiments represent \sim 50 cells per timepoint. Pearson's coefficient was calculated from 3 individual images. All data are displayed as means \pm SD.

Figure 4. Nanoparticle effects on lysosomal pH and protease activity. (A) Representative confocal images of lysosomal pH measurements using LysoSensor-Dextran Yellow/Blue in NP (\pm MFQ) 100 μ g/mL, free MFQ 10 μ M, bafilomycin 200 nM, or control treated Vero E6 cells. Scale bars=10 μ m. (B) Quantification of lysosomal pH. (C) Representative images of Calu-3 cells treated with NPs (\pm MFQ) 100 μ g/mL, free MFQ 20 μ M, bafilomycin 200 nM, or control and stained with Hoechst 33342 (blue) and LysoTracker Green (green) to probe for lysosome accumulation. Scale bars=20 μ m. (D) Quantification of lysosomal accumulation. (E) Quantification of lysosomal protease activity by DQ-Red BSA assay in Vero E6 cells treated with NPs (\pm MFQ), free MFQ, bafilomycin A1, pepstatin A + E64d, or controls at the indicated concentrations. Statistical significance was determined by one-way ANOVA: * p <0.05, ** p <0.01, *** p <0.001, **** p <0.0001 against untreated controls. All experiments represent n=3. All data are displayed as means \pm SEM.

Figure 5. PGC-NPs loaded with MFQ are effective at inhibiting MHV and HCoV-OC43 infection. (A) Schematic describing the treatment and infection sequence of prophylactic NP treated MHV-GFP or HCoV-OC43 infected cells. (B) Representative images of L929 cells pre-treated with control, remdesivir (RDV, 10 μ M), free MFQ (10 μ M), NPs (\pm MFQ) (100 μ g/mL) and infected with MHV-GFP (MOI 0.1) for 24 h. Nuclei were stained with DAPI (blue), and virus infected cells were visualized by GFP-positive signal (green) or syncytia formation. Scale bars=50 μ m. Quantification of cell numbers, GFP-area per image, and syncytia in unloaded NPs (C), MFQ-NPs (D) or free MFQ (E) treated cells. Statistical significance was determined by two-way ANOVA: a (at least) p <0.05 against MHV-Control cell numbers; b (at least) p <0.05 against MHV-Control infected cell area; c p <0.05 against MHV-Control syncytia count. (F) Representative images of Vero E6 cells pre-treated with control, RDV (10 μ M), free MFQ (20 μ M), NPs (\pm MFQ) (100 μ g/mL) and infected with HCoV-OC43 (MOI 1) for 48 h. Nuclei were stained with DAPI (blue), and virus infected cells were visualized by immunofluorescence staining against pan coronavirus nucleocapsid (green). Scale bars=50 μ m. (D) Quantification of cell numbers and fractions of infected cells in empty NP (G), MFQ-NP (H) or free MFQ (I) treated cells. Statistical significance was determined by two-way ANOVA: a (at least) p <0.05 against OC43-Control cell numbers; b (at least) p <0.05 against OC43-Control infected cell fraction. All experiments represent n=3. All data are displayed as means \pm SEM.

Figure 6. PGC-NPs loaded with MFQ are effective at inhibiting SARS-CoV-2 WT-WA1 and Omicron infection and replication. (A) Schematic describing the treatment and infection sequence of prophylactic NP treated SARS-CoV-2 infected cells. (B) Representative images of Calu-3 cells pre-treated with control,

RDV (10 μ M), free MFQ (20 μ M), NPs (\pm MFQ) (100 μ g/mL) and infected with SARS-CoV-2 WT-WA1 (MOI 0.2) for 48 h. Nuclei were stained with DAPI (blue) and virus infected cells visualized by immunofluorescence staining against SARS-CoV-2 N-protein (red). Scale bars=50 μ m. Quantification of cell numbers and fractions of infected cells in unloaded NP (C), MFQ-NP (D) or free MFQ (E) pretreated Calu-3 cells infected with SARS-CoV-2 WT-WA1. Quantification of cell numbers and fractions of infected cells in unloaded NP (F), MFQ-NP (G) or free MFQ (H) pretreated Calu-3 cells infected with SARS-CoV-2 Omicron BA.1. Statistical significance was determined by two-way ANOVA: a (at least) $p < 0.05$ against SARS-CoV-2 Control cell numbers; b (at least) $p < 0.05$ against SARS-CoV-2-Control infected cell area. (I) Schematic describing the treatment and infection sequence of SARS-CoV-2 infected cells treated after infection. Quantification of cell numbers and fractions of infected cells in unloaded NP (J), MFQ-NP (K) or free MFQ (L) treated Calu-3 cells infected with SARS-CoV-2 WT-WA1. Quantification of cell numbers and fractions of infected cells in unloaded NP (M), MFQ-NP (N) or free MFQ (O) treated Calu-3 cells infected with SARS-CoV-2 Omicron BA.1. Statistical significance was determined by two-way ANOVA: a (at least) $p < 0.05$ against SARS-CoV-2 Control cell numbers; b (at least) $p < 0.05$ against SARS-CoV-2-Control infected cell area. All experiments represent $n=3-4$. All data are displayed as means \pm SEM.

Supplemental Figure 1. (A) ^1H NMR (500 MHz, CDCl_3) spectrum of 5-benzyloxy-1,3-dioxan-2-one monomer. (B) ^1H NMR (500 MHz, CDCl_3) spectrum of poly(glycerol monostearate-co- ϵ -caprolactone) (PGC-C18) using a 4:1 molar ratio of ϵ -caprolactone to 5-benzyloxy-1,3-dioxan-2-one monomers. (C) THF GPC trace of PGC-C18. PGC-C18 molecular weight (M_n) = 78272 g/mol and dispersity (\mathcal{D}) = 1.668 were determined based on polystyrene standards according to refractive index (RI) detector.

Supplemental Figure 2. (Connected to Figures 1 and 2). (A) Quantification of cell numbers and fractions of infected cells in free molecular sulfadoxine pretreated Vero E6 cells infected with SARS-CoV-2 WT-WA1. (B) Quantification of cell numbers and fractions of infected cells in free molecular nitazoxanide pretreated Vero E6 cells infected with SARS-CoV-2 WT-WA1. (C) Electron micrograph of MFQ-NPs demonstrates consistent size and morphology. Scale Bar=200 nm. (D) Size distribution of MFQ-NPs measured by tunable resistive pulse sensing (i.e., qNano). (E) Effects of different concentrations of DMSO-vehicle treatments on HFL1, Vero E6, and Calu-3 cell viability measured by MTS assay. All experiments represent $n=3-4$. Sizing and dispersity data are displayed as means \pm SD; all other data are displayed as means \pm SEM.

Supplemental Figure 3. (Connected to Figures 3 and 4). (A) General pipeline outlining FlowJo gating of viable, single cells using forward and side scattering, resulting in histogram frequency distribution of individual cell fluorescence. Positive cell gating is based on unstained and untreated controls, representative unstained and stained controls from the DQ-Red BSA assay are shown. Rho-NP uptake measured by flow cytometry in Vero E6 cells and displayed as (B) representative intensity histogram or (C) mean intensity bar graph. Rho-NP uptake measured by flow cytometry in HFL1 cells and displayed as (D) representative intensity histogram or (E) mean intensity bar graph. (F) Representative images of Vero E6 cells treated with NPs \pm MFQ (100 μ g/mL), free MFQ (20 μ M), bafilomycin A1 (200 nM), or control and stained with Hoechst 33342 (blue) and LysoTracker Green (green) to probe for lysosome accumulation. Scale bars=20 μ m. (G) Quantification of lysosomal accumulation. Statistical significance was determined by one-way ANOVA: ** $p < 0.01$, *** $p < 0.001$, **** $p < 0.0001$ against Untreated controls. Flow cytometry

experiments represent n=6 and are displayed as means \pm SD. Imaging experiments represent n=3 and are displayed as means \pm SEM.

Supplemental Figure 4. (Connected to Figure 5). (A) Timeline of viral inoculation, GFP expression, and apoptosis in MHV-GFP infected L929 cells obtained by continuous image-based monitoring with a Cytosmart OmniFL analysis platform. Brightfield cell images are overlaid with GFP fluorescence (green) and Annexin V-Orange fluorescence (red). Scale bars=200 μ m. (B) Representative viral infection kinetic quantification over a 48 h infection period. (C) Representative example of syncytia (red outlines) recognized by CellProfiler analysis as clustered nuclei and GFP-positive area (yellow outlines) in fluorescence microscopy images obtained with the Operetta high-content imager. Nuclei (blue) are stained with DAPI, MHV (green) is visualized by GFP expression. GFP-negative syncytia are marked with white arrowheads. Scale bar=50 μ m.

Supplemental Figure 5. (Connected to Figure 6). (A) Schematic describing the treatment and infection sequence of prophylactic NP treated SARS-CoV-2 infected cells. (B) Representative images of Vero E6 cells pre-treated with control, RDV (10 μ M), free MFQ (20 μ M), NPs \pm MFQ (100 μ g/mL) and infected with SARS-CoV-2 WT-WA1 (MOI 0.1) for 48 h. Nuclei were stained with DAPI (blue) and virus infected cells visualized by immunofluorescence staining against SARS-CoV-2 N-protein (red). Scale bars=50 μ m. Quantification of cell numbers and fractions of infected cells in unloaded PGC-NP (C), MFQ-NP (D) or free MFQ (E) pretreated Vero E6 cells infected with SARS-CoV-2 WT-WA1. Statistical significance was determined by two-way ANOVA: a (at least) $p < 0.05$ against SARS-CoV-2 Control cell numbers; b (at least) $p < 0.05$ against SARS-CoV-2-Control infected cell area. Experiments represent n=3 and data are displayed as means \pm SEM.

REFERENCES

- Ader, F., M. Bouscambert-Duchamp, M. Hites, N. Peiffer-Smadja, J. Poissy, D. Belhadi, A. Diallo, M.-P. Lê, G. Peytavin, T. Staub, R. Greil, J. Guedj, J.-A. Paiva, D. Costagliola, Y. Yazdanpanah, C. Burdet, F. Mentré, A. Egle, R. Greil, M. Joannidis, B. Lamprecht, A. Altdorfer, L. Belkhir, V. Fraipont, M. Hites, G. Verschelden, J. Aboab, F. Ader, H. Ait-Oufella, C. Andrejak, P. Andreu, L. Argaud, F. Bani-Sadr, F. Benezit, M. Blot, E. Botelho-Nevers, L. Bouadma, O. Bouchaud, D. Bougon, K. Bouiller, F. Bounes-Vardon, D. Boutoille, A. Boyer, C. Bruel, A. Cabié, E. Canet, C. Cazanave, C. Chabartier, C. Chirouze, R. Clere-Jehl, J. Courjon, F. Crockett, F. Danion, A. Delbove, J. Dellamonica, F. Djossou, C. Dubost, A. Duvignaud, O. Epaulard, L. Epelboin, M. Fartoukh, K. Faure, E. Faure, T. Ferry, C. Ficko, S. Figueiredo, B. Gaborit, R. Gaci, A. Gagneux-Brunon, S. Gallien, D. Garot, G. Geri, S. Gibot, F. Goehringer, M. Gousseff, D. Gruson, Y. Hansmann, O. Hirschberger, S. Jaureguiberry, V. Jeanmichel, S. Kerneis, A. Kimmoun, K. Klouche, M. Lachâtre, K. Lacombe, F. Laine, J.-P. Lanoix, O. Launay, B. Laviolle, V. Le Moing, J. Le Pavec, Y. Le Tulzo, P. Le Turnier, D. Lebeaux, B. Lefevre, S. Leroy, F.-X. Lescure, H. Lessire, B. Leveau, P. Loubet, et al. 2022. Remdesivir plus standard of care versus standard of care alone for the treatment of patients admitted to hospital with COVID-19 (DisCoVeRy): a phase 3, randomised, controlled, open-label trial. *The Lancet Infectious Diseases*. 22:209-221.
- Agostini, M.L., A.J. Pruijssers, J.D. Chappell, J. Gribble, X. Lu, E.L. Andres, G.R. Bluemling, M.A. Lockwood, T.P. Sheahan, A.C. Sims, M.G. Natchus, M. Saindane, A.A. Kolykhalov, G.R. Painter, R.S. Baric, M.R. Denison, and T. Gallagher. 2019. Small-Molecule Antiviral β -d- N^4 -Hydroxycytidine Inhibits a Proofreading-Intact Coronavirus with a High Genetic Barrier to Resistance. *Journal of Virology*. 93.
- Akazawa, D., H. Ohashi, T. Hishiki, T. Morita, S. Iwanami, K.S. Kim, Y.D. Jeong, E.-S. Park, M. Kataoka, K. Shionoya, J. Mifune, K. Tsuchimoto, S. Ojima, A.H. Azam, S. Nakajima, H. Park, T. Yoshikawa, M. Shimojima, K. Kiga, S. Iwami, K. Maeda, T. Suzuki, H. Ebihara, Y. Takahashi, and K. Watashi. 2023. Potential Anti-Mpox Virus Activity of Atovaquone, Mefloquine, and Molnupiravir, and Their Potential Use as Treatments. *The Journal of Infectious Diseases*.
- Al-Halifa, S., L. Gauthier, D. Arpin, S. Bourgault, and D. Archambault. 2019. Nanoparticle-Based Vaccines Against Respiratory Viruses. *Frontiers in Immunology*. 10.
- Arshad, U., H. Pertinez, H. Box, L. Tatham, R.K.R. Rajoli, P. Curley, M. Neary, J. Sharp, N.J. Liptrott, A. Valentijn, C. David, S.P. Rannard, P.M. O'Neill, G. Aljayyousi, S.H. Pennington, S.A. Ward, A. Hill, D.J. Back, S.H. Khoo, P.G. Bray, G.A. Biagini, and A. Owen. 2020. Prioritization of Anti-SARS-Cov-2 Drug Repurposing Opportunities Based on Plasma and Target Site Concentrations Derived from their Established Human Pharmacokinetics. *Clinical Pharmacology & Therapeutics*. 108:775-790.
- Baden, L.R., H.M. El Sahly, B. Essink, K. Kotloff, S. Frey, R. Novak, D. Diemert, S.A. Spector, N. Roupael, C.B. Creech, J. McGettigan, S. Khetan, N. Segall, J. Solis, A. Brosz, C. Fierro, H. Schwartz, K. Neuzil, L. Corey, P. Gilbert, H. Janes, D. Follmann, M. Marovich, J. Mascola, L. Polakowski, J. Ledgerwood, B.S. Graham, H. Bennett, R. Pajon, C. Knightly, B. Leav, W. Deng, H. Zhou, S. Han, M. Ivarsson, J. Miller, T. Zaks, and C.S. Group. 2021. Efficacy and Safety of the mRNA-1273 SARS-CoV-2 Vaccine. *N Engl J Med*. 384:403-416.

- Balasubramanian, A., T. Teramoto, A.A. Kulkarni, A.K. Bhattacharjee, and R. Padmanabhan. 2017. Antiviral activities of selected antimalarials against dengue virus type 2 and Zika virus. *Antiviral Res.* 137:141-150.
- Baum, A., D. Ajithdoss, R. Copin, A. Zhou, K. Lanza, N. Negron, M. Ni, Y. Wei, K. Mohammadi, B. Musser, G.S. Atwal, A. Oyejide, Y. Goetz-Gazi, J. Dutton, E. Clemmons, H.M. Staples, C. Bartley, B. Klaffke, K. Alfson, M. Gazi, O. Gonzalez, E. Dick, R. Carrion, L. Pessaint, M. Porto, A. Cook, R. Brown, V. Ali, J. Greenhouse, T. Taylor, H. Andersen, M.G. Lewis, N. Stahl, A.J. Murphy, G.D. Yancopoulos, and C.A. Kyratsous. 2020. REGN-COV2 antibodies prevent and treat SARS-CoV-2 infection in rhesus macaques and hamsters. *Science.* 370:1110-1115.
- Beigel, J.H., K.M. Tomashek, L.E. Dodd, A.K. Mehta, B.S. Zingman, A.C. Kalil, E. Hohmann, H.Y. Chu, A. Luetkemeyer, S. Kline, D. Lopez de Castilla, R.W. Finberg, K. Dierberg, V. Tapson, L. Hsieh, T.F. Patterson, R. Paredes, D.A. Sweeney, W.R. Short, G. Touloumi, D.C. Lye, N. Ohmagari, M.-d. Oh, G.M. Ruiz-Palacios, T. Benfield, G. Fätkenheuer, M.G. Kortepeter, R.L. Atmar, C.B. Creech, J. Lundgren, A.G. Babiker, S. Pett, J.D. Neaton, T.H. Burgess, T. Bonnett, M. Green, M. Makowski, A. Osinusi, S. Nayak, and H.C. Lane. 2020. Remdesivir for the Treatment of Covid-19 — Final Report. *New England Journal of Medicine.* 383:1813-1826.
- Blum, V.F., S. Cimerman, J.R. Hunter, P. Tierno, A. Lacerda, A. Soeiro, F. Cardoso, N.C. Bellei, J. Maricato, N. Mantovani, M. Vassao, D. Dias, J. Galinskas, L.M.R. Janini, J.R. Santos-Oliveira, A.M. Da-Cruz, and R.S. Diaz. 2021. Nitazoxanide superiority to placebo to treat moderate COVID-19 – A Pilot prove of concept randomized double-blind clinical trial. *eClinicalMedicine.* 37.
- Calabrese, E.J., J.C. Hanekamp, Y.N. Hanekamp, R. Kapoor, G. Dhawan, and E. Agathokleous. 2021. Chloroquine commonly induces hormetic dose responses. *Science of The Total Environment.* 755.
- Cao, B., Y. Wang, D. Wen, W. Liu, J. Wang, G. Fan, L. Ruan, B. Song, Y. Cai, M. Wei, X. Li, J. Xia, N. Chen, J. Xiang, T. Yu, T. Bai, X. Xie, L. Zhang, C. Li, Y. Yuan, H. Chen, H. Li, H. Huang, S. Tu, F. Gong, Y. Liu, Y. Wei, C. Dong, F. Zhou, X. Gu, J. Xu, Z. Liu, Y. Zhang, H. Li, L. Shang, K. Wang, K. Li, X. Zhou, X. Dong, Z. Qu, S. Lu, X. Hu, S. Ruan, S. Luo, J. Wu, L. Peng, F. Cheng, L. Pan, J. Zou, C. Jia, J. Wang, X. Liu, S. Wang, X. Wu, Q. Ge, J. He, H. Zhan, F. Qiu, L. Guo, C. Huang, T. Jaki, F.G. Hayden, P.W. Horby, D. Zhang, and C. Wang. 2020. A Trial of Lopinavir–Ritonavir in Adults Hospitalized with Severe Covid-19. *New England Journal of Medicine.* 382:1787-1799.
- Carpenter, A.E., T.R. Jones, M.R. Lamprecht, C. Clarke, I. Kang, O. Friman, D.A. Guertin, J. Chang, R.A. Lindquist, J. Moffat, P. Golland, and D.M. Sabatini. 2006. CellProfiler: image analysis software for identifying and quantifying cell phenotypes. *Genome Biology.* 7.
- Chen, D., Q. Zheng, L. Sun, M. Ji, Y. Li, H. Deng, and H. Zhang. 2021. ORF3a of SARS-CoV-2 promotes lysosomal exocytosis-mediated viral egress. *Developmental Cell.* 56:3250-3263.e3255.
- Coowanitwong, I., V. Arya, P. Kulvanich, and G. Hochhaus. 2008. Slow Release Formulations of Inhaled Rifampin. *The AAPS Journal.* 10:342-348.
- Cortese, M., J.-Y. Lee, B. Cerikan, C.J. Neufeldt, V.M.J. Oorschot, S. Köhrer, J. Hennies, N.L. Schieber, P. Ronchi, G. Mizzon, I. Romero-Brey, R. Santarella-Mellwig, M. Schorb, M. Boermel, K. Mocaer, M.S. Beckwith, R.M. Templin, V. Gross, C. Pape, C. Tischer, J. Frankish, N.K. Horvat, V. Laketa, M.

- Stanifer, S. Boulant, A. Ruggieri, L. Chatel-Chaix, Y. Schwab, and R. Bartenschlager. 2020. Integrative Imaging Reveals SARS-CoV-2-Induced Reshaping of Subcellular Morphologies. *Cell Host & Microbe*. 28:853-866.e855.
- Cowley, T.J., and S.R. Weiss. 2010. Murine coronavirus neuropathogenesis: determinants of virulence. *J Neurovirol*. 16:427-434.
- Dodd, E.L., and D.S. Bohle. 2014. Orienting the heterocyclic periphery: a structural model for chloroquine's antimalarial activity. *Chem. Commun*. 50:13765-13768.
- Dong, E., H. Du, and L. Gardner. 2020. An interactive web-based dashboard to track COVID-19 in real time. *Lancet Infect Dis*. 20:533-534.
- Dougan, M., A. Nirula, M. Azizad, B. Mocherla, R.L. Gottlieb, P. Chen, C. Hebert, R. Perry, J. Boscia, B. Heller, J. Morris, C. Crystal, A. Igbinalolor, G. Huhn, J. Cardona, I. Shawa, P. Kumar, A.C. Adams, J. Van Naarden, K.L. Custer, M. Durante, G. Oakley, A.E. Schade, T.R. Holzer, P.J. Ebert, R.E. Higgs, N.L. Kallewaard, J. Sabo, D.R. Patel, M.C. Dabora, P. Klekotka, L. Shen, and D.M. Skovronsky. 2021. Bamlanivimab plus Etesevimab in Mild or Moderate Covid-19. *New England Journal of Medicine*. 385:1382-1392.
- Ekladios, I., R. Liu, H. Zhang, D.H. Foil, D.A. Todd, T.N. Graf, R.F. Padera, N.H. Oberlies, Y.L. Colson, and M.W. Grinstaff. 2017. Synthesis of poly(1,2-glycerol carbonate)-paclitaxel conjugates and their utility as a single high-dose replacement for multi-dose treatment regimens in peritoneal cancer. *Chemical Science*. 8:8443-8450.
- Garcia-Beltran, W.F., E.C. Lam, K. St Denis, A.D. Nitido, Z.H. Garcia, B.M. Hauser, J. Feldman, M.N. Pavlovic, D.J. Gregory, M.C. Poznansky, A. Sigal, A.G. Schmidt, A.J. Iafrate, V. Naranbhai, and A.B. Balazs. 2021. Multiple SARS-CoV-2 variants escape neutralization by vaccine-induced humoral immunity. *Cell*. 184:2523.
- Geiser, M., and W.G. Kreyling. 2010. Deposition and biokinetics of inhaled nanoparticles. *Particle and Fibre Toxicology*. 7.
- Golden, E.B., H.Y. Cho, F.M. Hofman, S.G. Louie, A.H. Schonthal, and T.C. Chen. 2015. Quinoline-based antimalarial drugs: a novel class of autophagy inhibitors. *Neurosurg Focus*. 38:E12.
- Goldman, J.D., D.C.B. Lye, D.S. Hui, K.M. Marks, R. Bruno, R. Montejano, C.D. Spinner, M. Galli, M.Y. Ahn, R.G. Nahass, Y.S. Chen, D. SenGupta, R.H. Hyland, A.O. Osinusi, H. Cao, C. Blair, X. Wei, A. Gaggar, D.M. Brainard, W.J. Towner, J. Munoz, K.M. Mullane, F.M. Marty, K.T. Tashima, G. Diaz, A. Subramanian, and G.-U.-. Investigators. 2020. Remdesivir for 5 or 10 Days in Patients with Severe Covid-19. *N Engl J Med*. 383:1827-1837.
- Gottlieb, R.L., A. Nirula, P. Chen, J. Boscia, B. Heller, J. Morris, G. Huhn, J. Cardona, B. Mocherla, V. Stosor, I. Shawa, P. Kumar, A.C. Adams, J. Van Naarden, K.L. Custer, M. Durante, G. Oakley, A.E. Schade, T.R. Holzer, P.J. Ebert, R.E. Higgs, N.L. Kallewaard, J. Sabo, D.R. Patel, P. Klekotka, L. Shen, and D.M. Skovronsky. 2021. Effect of Bamlanivimab as Monotherapy or in Combination With Etesevimab on Viral Load in Patients With Mild to Moderate COVID-19. *Jama*. 325.

- Gottlieb, R.L., C.E. Vaca, R. Paredes, J. Mera, B.J. Webb, G. Perez, G. Oguchi, P. Ryan, B.U. Nielsen, M. Brown, A. Hidalgo, Y. Sachdeva, S. Mittal, O. Osiyemi, J. Skarbinski, K. Juneja, R.H. Hyland, A. Osinusi, S. Chen, G. Camus, M. Abdelghany, S. Davies, N. Behenna-Renton, F. Duff, F.M. Marty, M.J. Katz, A.A. Ginde, S.M. Brown, J.T. Schiffer, and J.A. Hill. 2022. Early Remdesivir to Prevent Progression to Severe Covid-19 in Outpatients. *New England Journal of Medicine*. 386:305-315.
- Group, T.R.C. 2020. Effect of Hydroxychloroquine in Hospitalized Patients with Covid-19. *New England Journal of Medicine*. 383:2030-2040.
- Gupta, A., Y. Gonzalez-Rojas, E. Juarez, M. Crespo Casal, J. Moya, D.R. Falci, E. Sarkis, J. Solis, H. Zheng, N. Scott, A.L. Cathcart, C.M. Hebner, J. Sager, E. Mogalian, C. Tipple, A. Peppercorn, E. Alexander, P.S. Pang, A. Free, C. Brinson, M. Aldinger, and A.E. Shapiro. 2021. Early Treatment for Covid-19 with SARS-CoV-2 Neutralizing Antibody Sotrovimab. *New England Journal of Medicine*. 385:1941-1950.
- Gupta, A., Y. Gonzalez-Rojas, E. Juarez, M. Crespo Casal, J. Moya, D. Rodrigues Falci, E. Sarkis, J. Solis, H. Zheng, N. Scott, A.L. Cathcart, S. Parra, J.E. Sager, D. Austin, A. Peppercorn, E. Alexander, W.W. Yeh, C. Brinson, M. Aldinger, A.E. Shapiro, A. Free, K. Johnson, E. Cordasco, R. Little, A. Bajwa, A. Doshi, A. Focil, R. Hussain, G. Bostick, G. Somodevilla, H. Ali, J. Kowalczyk, S. Mittal, J. Caso, M. Gousse, L. Espinal, L. Zepeda, T. Nguyen, L. Martinez, G. Alvarez, R. Pucillo, M. Seep, N. Parikh, V. Escobar, A. Curra, V. Dal Maso, J. O'Mahony, E. Ramacciotti, J. Diaz, K. Luz, P. Ruane, B. Mochlera, J. Roldan Sanchez, L. Hernandez, A. Fernandez, G. Leavitt, M. Azizad, H. Afzal, A. Fatakia, S. Narejos Perez, C.M. Stadnik, L. Gorgos, Y. Sachdeva, P. Segura, C. Quandros, R. Perry, and L. Sher. 2022. Effect of Sotrovimab on Hospitalization or Death Among High-risk Patients With Mild to Moderate COVID-19. *Jama*. 327.
- Hammond, J., H. Leister-Tebbe, A. Gardner, P. Abreu, W. Bao, W. Wisemandle, M. Baniecki, V.M. Hendrick, B. Damle, A. Simón-Campos, R. Pypstra, and J.M. Rusnak. 2022. Oral Nirmatrelvir for High-Risk, Nonhospitalized Adults with Covid-19. *New England Journal of Medicine*. 386:1397-1408.
- He, S., J. Gui, K. Xiong, M. Chen, H. Gao, and Y. Fu. 2022. A roadmap to pulmonary delivery strategies for the treatment of infectious lung diseases. *Journal of Nanobiotechnology*. 20.
- Heil, E.L., and S. Kottlilil. 2022. The Goldilocks Time for Remdesivir — Is Any Indication Just Right? *New England Journal of Medicine*. 386:385-387.
- Heilmann, E., F. Costacurta, S.A. Moghadasi, C. Ye, M. Pavan, D. Bassani, A. Volland, C. Ascher, A.K.H. Weiss, D. Bante, R.S. Harris, S. Moro, B. Rupp, L. Martinez-Sobrido, and D. von Laer. 2022. SARS-CoV-2 3CL^{pro} mutations selected in a VSV-based system confer resistance to nirmatrelvir, ensitrelvir, and GC376. *Science Translational Medicine*.
- Hoffmann, M., K. Mösbauer, H. Hofmann-Winkler, A. Kaul, H. Kleine-Weber, N. Krüger, N.C. Gassen, M.A. Müller, C. Drosten, and S. Pöhlmann. 2020. Chloroquine does not inhibit infection of human lung cells with SARS-CoV-2. *Nature*. 585:588-590.
- Hoppe, H.C., D.A. van Schalkwyk, U.I. Wiehart, S.A. Meredith, J. Egan, and B.W. Weber. 2004. Antimalarial quinolines and artemisinin inhibit endocytosis in *Plasmodium falciparum*. *Antimicrob Agents Chemother*. 48:2370-2378.

- Horby, P.W., M. Mafham, J.L. Bell, L. Linsell, N. Staplin, J. Emberson, A. Palfreeman, J. Raw, E. Elmahi, B. Prudon, C. Green, S. Carley, D. Chadwick, M. Davies, M.P. Wise, J.K. Baillie, L.C. Chappell, S.N. Faust, T. Jaki, K. Jefferey, W.S. Lim, A. Montgomery, K. Rowan, E. Juszczak, R. Haynes, and M.J. Landray. 2020. Lopinavir–ritonavir in patients admitted to hospital with COVID-19 (RECOVERY): a randomised, controlled, open-label, platform trial. *The Lancet*. 396:1345-1352.
- Jan, J.T., T.R. Cheng, Y.P. Juang, H.H. Ma, Y.T. Wu, W.B. Yang, C.W. Cheng, X. Chen, T.H. Chou, J.J. Shie, W.C. Cheng, R.J. Chein, S.S. Mao, P.H. Liang, C. Ma, S.C. Hung, and C.H. Wong. 2021. Identification of existing pharmaceuticals and herbal medicines as inhibitors of SARS-CoV-2 infection. *Proc Natl Acad Sci U S A*. 118.
- Jayk Bernal, A., M.M. Gomes da Silva, D.B. Musungaie, E. Kovalchuk, A. Gonzalez, V. Delos Reyes, A. Martín-Quirós, Y. Caraco, A. Williams-Diaz, M.L. Brown, J. Du, A. Pedley, C. Assaid, J. Strizki, J.A. Grobler, H.H. Shamsuddin, R. Tipping, H. Wan, A. Paschke, J.R. Butterson, M.G. Johnson, and C. De Anda. 2022. Molnupiravir for Oral Treatment of Covid-19 in Nonhospitalized Patients. *New England Journal of Medicine*. 386:509-520.
- Jochmans, D., C. Liu, K. Donckers, A. Stoycheva, S. Boland, S.K. Stevens, C. De Vita, B. Vanmechelen, P. Maes, B. Trüeb, N. Ebert, V. Thiel, S. De Jonghe, L. Vangeel, D. Bardiot, A. Jekle, L.M. Blatt, L. Beigelman, J.A. Symons, P. Raboisson, P. Chaltin, A. Marchand, J. Neyts, J. Deval, and K. Vandyck. 2022. The substitutions L50F, E166A and L167F in SARS-CoV-2 3CLpro are selected by a protease inhibitor in vitro and confer resistance to nirmatrelvir. *bioRxiv*.
- Kabinger, F., C. Stiller, J. Schmitzová, C. Dienemann, G. Kokic, H.S. Hillen, C. Höbartner, and P. Cramer. 2021. Mechanism of molnupiravir-induced SARS-CoV-2 mutagenesis. *Nature Structural & Molecular Biology*. 28:740-746.
- Kaplan, J.A., R. Liu, J.D. Freedman, R. Padera, J. Schwartz, Y.L. Colson, and M.W. Grinstaff. 2016. Prevention of lung cancer recurrence using cisplatin-loaded superhydrophobic nanofiber meshes. *Biomaterials*. 76:273-281.
- Karbwang, J., and N.J. White. 1990. Clinical Pharmacokinetics of Mefloquine. *Clinical Pharmacokinetics*. 19:264-279.
- Lee, B., T. Ou, H. Mou, L. Zhang, A. Ojha, H. Choe, and M. Farzan. 2021. Hydroxychloroquine-mediated inhibition of SARS-CoV-2 entry is attenuated by TMPRSS2. *PLOS Pathogens*. 17.
- Liu, J., R. Cao, M. Xu, X. Wang, H. Zhang, H. Hu, Y. Li, Z. Hu, W. Zhong, and M. Wang. 2020. Hydroxychloroquine, a less toxic derivative of chloroquine, is effective in inhibiting SARS-CoV-2 infection in vitro. *Cell Discovery*. 6.
- Liu, J., Y. Li, Q. Liu, Q. Yao, X. Wang, H. Zhang, R. Chen, L. Ren, J. Min, F. Deng, B. Yan, L. Liu, Z. Hu, M. Wang, and Y. Zhou. 2021. SARS-CoV-2 cell tropism and multiorgan infection. *Cell Discovery*. 7.
- Lokhande, A.S., and P.V. Devarajan. 2021. A review on possible mechanistic insights of Nitazoxanide for repurposing in COVID-19. *European Journal of Pharmacology*. 891.

- Löndahl, J., W. Möller, J.H. Pagels, W.G. Kreyling, E. Swietlicki, and O. Schmid. 2014. Measurement Techniques for Respiratory Tract Deposition of Airborne Nanoparticles: A Critical Review. *Journal of Aerosol Medicine and Pulmonary Drug Delivery*. 27:229-254.
- Mahmoud, D.B., Z. Shitu, and A. Mostafa. 2020. Drug repurposing of nitazoxanide: can it be an effective therapy for COVID-19? *Journal of Genetic Engineering and Biotechnology*. 18.
- Martins, A.C., M.M.B. Paoliello, A.O. Docea, A. Santamaria, A.A. Tinkov, A.V. Skalny, and M. Aschner. 2021. Review of the mechanism underlying mefloquine-induced neurotoxicity. *Critical Reviews in Toxicology*. 51:209-216.
- McCarthy, S. 2015. Malaria Prevention, Mefloquine Neurotoxicity, Neuropsychiatric Illness, and Risk-Benefit Analysis in the Australian Defence Force. *Journal of Parasitology Research*. 2015:1-23.
- McLachlan, A.J., S.E. Tett, D.J. Cutler, and R.O. Day. 1993. Absorption and in vivo dissolution of hydroxychloroquine in fed subjects assessed using deconvolution techniques. *British Journal of Clinical Pharmacology*. 36:405-411.
- Miller, K., M.E. McGrath, Z. Hu, S. Ariannejad, S. Weston, M. Frieman, and W.T. Jackson. 2020. Coronavirus interactions with the cellular autophagy machinery. *Autophagy*. 16:2131-2139.
- Moore, M.N. 2020. Lysosomes, Autophagy, and Hormesis in Cell Physiology, Pathology, and Age-Related Disease. *Dose-Response*. 18.
- Münz, C. 2017. The Autophagic Machinery in Viral Exocytosis. *Frontiers in Microbiology*. 8.
- Nicola, M., Z. Alsafi, C. Sohrabi, A. Kerwan, A. Al-Jabir, C. Iosifidis, M. Agha, and R. Agha. 2020. The socio-economic implications of the coronavirus pandemic (COVID-19): A review. *Int J Surg*. 78:185-193.
- Owen, D.R., C.M.N. Allerton, A.S. Anderson, L. Aschenbrenner, M. Avery, S. Berritt, B. Boras, R.D. Cardin, A. Carlo, K.J. Coffman, A. Dantonio, L. Di, H. Eng, R. Ferre, K.S. Gajiwala, S.A. Gibson, S.E. Greasley, B.L. Hurst, E.P. Kadar, A.S. Kalgutkar, J.C. Lee, J. Lee, W. Liu, S.W. Mason, S. Noell, J.J. Novak, R.S. Obach, K. Ogilvie, N.C. Patel, M. Pettersson, D.K. Rai, M.R. Reese, M.F. Sammons, J.G. Sathish, R.S.P. Singh, C.M. Stepan, A.E. Stewart, J.B. Tuttle, L. Updyke, P.R. Verhoest, L. Wei, Q. Yang, and Y. Zhu. 2021. An oral SARS-CoV-2 M^{pro} inhibitor clinical candidate for the treatment of COVID-19. *Science*. 374:1586-1593.
- Patel, T.K., P.B. Patel, M. Barvaliya, M.K. Saurabh, H.L. Bhalla, and P.P. Khosla. 2021. Efficacy and safety of lopinavir-ritonavir in COVID-19: A systematic review of randomized controlled trials. *Journal of Infection and Public Health*. 14:740-748.
- Polack, F.P., S.J. Thomas, N. Kitchin, J. Absalon, A. Gurtman, S. Lockhart, J.L. Perez, G. Perez Marc, E.D. Moreira, C. Zerbini, R. Bailey, K.A. Swanson, S. Roychoudhury, K. Koury, P. Li, W.V. Kalina, D. Cooper, R.W. Frenck, Jr., L.L. Hammitt, O. Tureci, H. Nell, A. Schaefer, S. Unal, D.B. Tresnan, S. Mather, P.R. Dormitzer, U. Sahin, K.U. Jansen, W.C. Gruber, and C.C.T. Group. 2020. Safety and Efficacy of the BNT162b2 mRNA Covid-19 Vaccine. *N Engl J Med*. 383:2603-2615.

- Ramsey, J.D., I.E. Stewart, E.A. Madden, C. Lim, D. Hwang, M.T. Heise, A.J. Hickey, and A.V. Kabanov. 2022. Nanoformulated Remdesivir with Extremely Low Content of Poly(2-oxazoline)-Based Stabilizer for Aerosol Treatment of COVID-19. *Macromolecular Bioscience*. 22.
- Ryu, S., I. Shchukina, Y.-H. Youm, H. Qing, B. Hilliard, T. Dlugos, X. Zhang, Y. Yasumoto, C.J. Booth, C. Fernández-Hernando, Y. Suárez, K. Khanna, T.L. Horvath, M.O. Dietrich, M. Artyomov, A. Wang, and V.D. Dixit. 2021. Ketogenic diet restrains aging-induced exacerbation of coronavirus infection in mice. *eLife*. 10.
- Sacramento, C.Q., N. Fintelman-Rodrigues, S.S.G. Dias, J.R. Temerozo, A.d.P.D. Da Silva, C.S. da Silva, C. Blanco, A.C. Ferreira, M. Mattos, V.C. Soares, F. Pereira-Dutra, M.D. Miranda, D.F. Barreto-Vieira, M.A.N. da Silva, S.S. Santos, M. Torres, O.A. Chaves, R.K.R. Rajoli, A. Paccanaro, A. Owen, D.C. Bou-Habib, P.T. Bozza, and T.M.L. Souza. 2022. Unlike Chloroquine, Mefloquine Inhibits SARS-CoV-2 Infection in Physiologically Relevant Cells. *Viruses*. 14.
- Serafin, M.B., A. Bottega, V.S. Foletto, T.F. da Rosa, A. Horner, and R. Horner. 2020. Drug repositioning is an alternative for the treatment of coronavirus COVID-19. *Int J Antimicrob Agents*. 55:105969.
- Sharma, N., S. Thomas, E.B. Golden, F.M. Hofman, T.C. Chen, N.A. Petasis, A.H. Schonthal, and S.G. Louie. 2012. Inhibition of autophagy and induction of breast cancer cell death by mefloquine, an antimalarial agent. *Cancer Lett*. 326:143-154.
- Shin, J.H., D.J. Bae, E.S. Kim, H.B. Kim, S.J. Park, Y.K. Jo, D.S. Jo, D.G. Jo, S.Y. Kim, and D.H. Cho. 2015. Autophagy Regulates Formation of Primary Cilia in Mefloquine-Treated Cells. *Biomol Ther (Seoul)*. 23:327-332.
- Shionoya, K., M. Yamasaki, S. Iwanami, Y. Ito, S. Fukushi, H. Ohashi, W. Saso, T. Tanaka, S. Aoki, K. Kuramochi, S. Iwami, Y. Takahashi, T. Suzuki, M. Muramatsu, M. Takeda, T. Wakita, and K. Watashi. 2021. Mefloquine, a Potent Anti-severe Acute Respiratory Syndrome-Related Coronavirus 2 (SARS-CoV-2) Drug as an Entry Inhibitor in vitro. *Frontiers in Microbiology*. 12.
- Spinner, C.D., R.L. Gottlieb, G.J. Criner, J.R. Arribas Lopez, A.M. Cattelan, A. Soriano Viladomiu, O. Ogbuagu, P. Malhotra, K.M. Mullane, A. Castagna, L.Y.A. Chai, M. Roestenberg, O.T.Y. Tsang, E. Bernasconi, P. Le Turnier, S.C. Chang, D. SenGupta, R.H. Hyland, A.O. Osinusi, H. Cao, C. Blair, H. Wang, A. Gaggar, D.M. Brainard, M.J. McPhail, S. Bhagani, M.Y. Ahn, A.J. Sanyal, G. Huhn, F.M. Marty, and G.-U.-. Investigators. 2020. Effect of Remdesivir vs Standard Care on Clinical Status at 11 Days in Patients With Moderate COVID-19: A Randomized Clinical Trial. *JAMA*. 324:1048-1057.
- Stevens, L.J., A.J. Pruijssers, H.W. Lee, C.J. Gordon, E.P. Tchesnokov, J. Gribble, A.S. George, T.M. Hughes, X. Lu, J. Li, J.K. Perry, D.P. Porter, T. Cihlar, T.P. Sheahan, R.S. Baric, M. Götte, and M.R. Denison. 2022. Mutations in the SARS-CoV-2 RNA-dependent RNA polymerase confer resistance to remdesivir by distinct mechanisms. *Science Translational Medicine*. 14.
- Thorley, A.J., P. Ruenraroengsak, T.E. Potter, and T.D. Tetley. 2014. Critical Determinants of Uptake and Translocation of Nanoparticles by the Human Pulmonary Alveolar Epithelium. *ACS Nano*. 8:11778-11789.

- Tleyjeh, I.M., Z. Kashour, O. AlDosary, M. Riaz, H. Tlayjeh, M.A. Garbati, R. Tleyjeh, M.H. Al-Mallah, M.R. Sohail, D. Gerberi, A.A. Bin Abdulhak, J.R. Giudicessi, M.J. Ackerman, and T. Kashour. 2021. Cardiac Toxicity of Chloroquine or Hydroxychloroquine in Patients With COVID-19: A Systematic Review and Meta-regression Analysis. *Mayo Clinic Proceedings: Innovations, Quality & Outcomes*. 5:137-150.
- Touret, F., M. Gilles, K. Barral, A. Nougairède, J. van Helden, E. Decroly, X. de Lamballerie, and B. Coutard. 2020. In vitro screening of a FDA approved chemical library reveals potential inhibitors of SARS-CoV-2 replication. *Scientific Reports*. 10.
- Ungaro, F., I. d'Angelo, C. Coletta, R. d'Emmanuele di Villa Bianca, R. Sorrentino, B. Perfetto, M.A. Tufano, A. Miro, M.I. La Rotonda, and F. Quaglia. 2012. Dry powders based on PLGA nanoparticles for pulmonary delivery of antibiotics: Modulation of encapsulation efficiency, release rate and lung deposition pattern by hydrophilic polymers. *Journal of Controlled Release*. 157:149-159.
- Vartak, R., S.M. Patil, A. Saraswat, M. Patki, N.K. Kunda, and K. Patel. 2021. Aerosolized nanoliposomal carrier of remdesivir: an effective alternative for COVID-19 treatment in vitro. *Nanomedicine*. 16:1187-1202.
- Wang, M., R. Cao, L. Zhang, X. Yang, J. Liu, M. Xu, Z. Shi, Z. Hu, W. Zhong, and G. Xiao. 2020. Remdesivir and chloroquine effectively inhibit the recently emerged novel coronavirus (2019-nCoV) in vitro. *Cell Research*. 30:269-271.
- Weinreich, D.M., S. Sivapalasingam, T. Norton, S. Ali, H. Gao, R. Bhore, B.J. Musser, Y. Soo, D. Rofail, J. Im, C. Perry, C. Pan, R. Hosain, A. Mahmood, J.D. Davis, K.C. Turner, A.T. Hooper, J.D. Hamilton, A. Baum, C.A. Kyratsous, Y. Kim, A. Cook, W. Kampman, A. Kohli, Y. Sachdeva, X. Graber, B. Kowal, T. DiCioccio, N. Stahl, L. Lipsich, N. Braunstein, G. Herman, and G.D. Yancopoulos. 2021a. REGN-COV2, a Neutralizing Antibody Cocktail, in Outpatients with Covid-19. *New England Journal of Medicine*. 384:238-251.
- Weinreich, D.M., S. Sivapalasingam, T. Norton, S. Ali, H. Gao, R. Bhore, J. Xiao, A.T. Hooper, J.D. Hamilton, B.J. Musser, D. Rofail, M. Hussein, J. Im, D.Y. Atmodjo, C. Perry, C. Pan, A. Mahmood, R. Hosain, J.D. Davis, K.C. Turner, A. Baum, C.A. Kyratsous, Y. Kim, A. Cook, W. Kampman, L. Roque-Guerrero, G. Acloque, H. Aazami, K. Cannon, J.A. Simón-Campos, J.A. Bocchini, B. Kowal, A.T. DiCioccio, Y. Soo, G.P. Geba, N. Stahl, L. Lipsich, N. Braunstein, G. Herman, and G.D. Yancopoulos. 2021b. REGEN-COV Antibody Combination and Outcomes in Outpatients with Covid-19. *New England Journal of Medicine*. 385.
- WHO. 2021. Repurposed Antiviral Drugs for Covid-19 — Interim WHO Solidarity Trial Results. *New England Journal of Medicine*. 384:497-511.
- WHO. 2023. Weekly epidemiological update on COVID-19 - 20 April 2023.
- Xie, Y., J. Zhang, B. Lu, Z. Bao, J. Zhao, X. Lu, Y. Wei, K. Yao, Y. Jiang, Q. Yuan, X. Zhang, B. Li, X. Chen, Z. Dong, and K. Liu. 2020. Mefloquine Inhibits Esophageal Squamous Cell Carcinoma Tumor Growth by Inducing Mitochondrial Autophagy. *Front Oncol*. 10:1217.

Figure 1

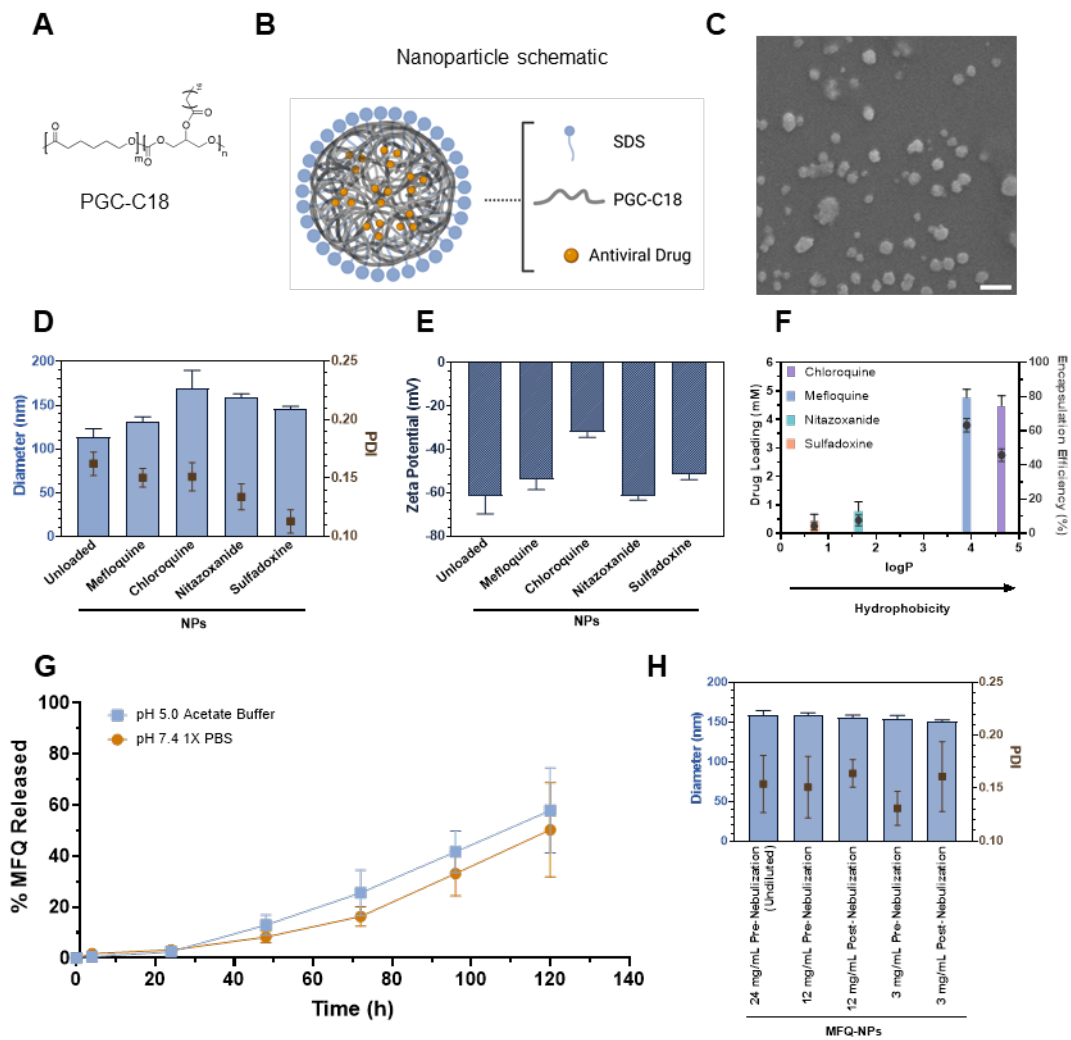


Figure 2

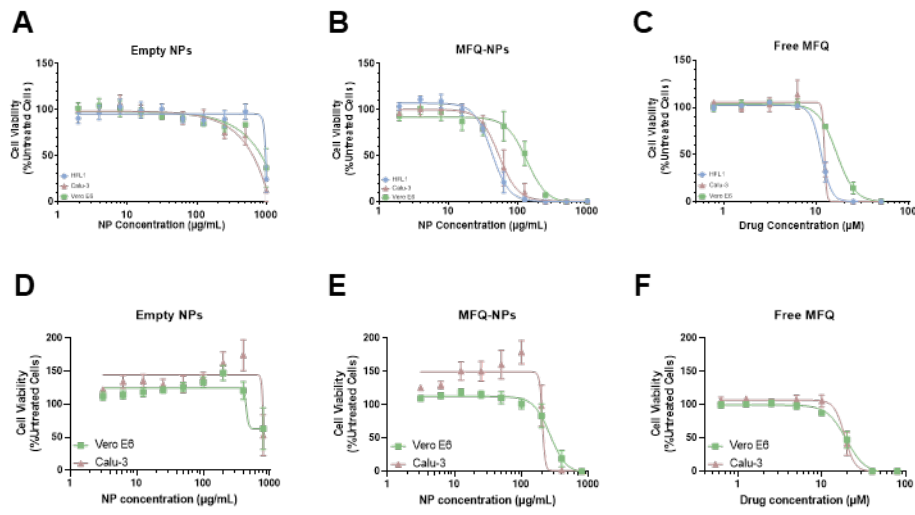


Figure 3.

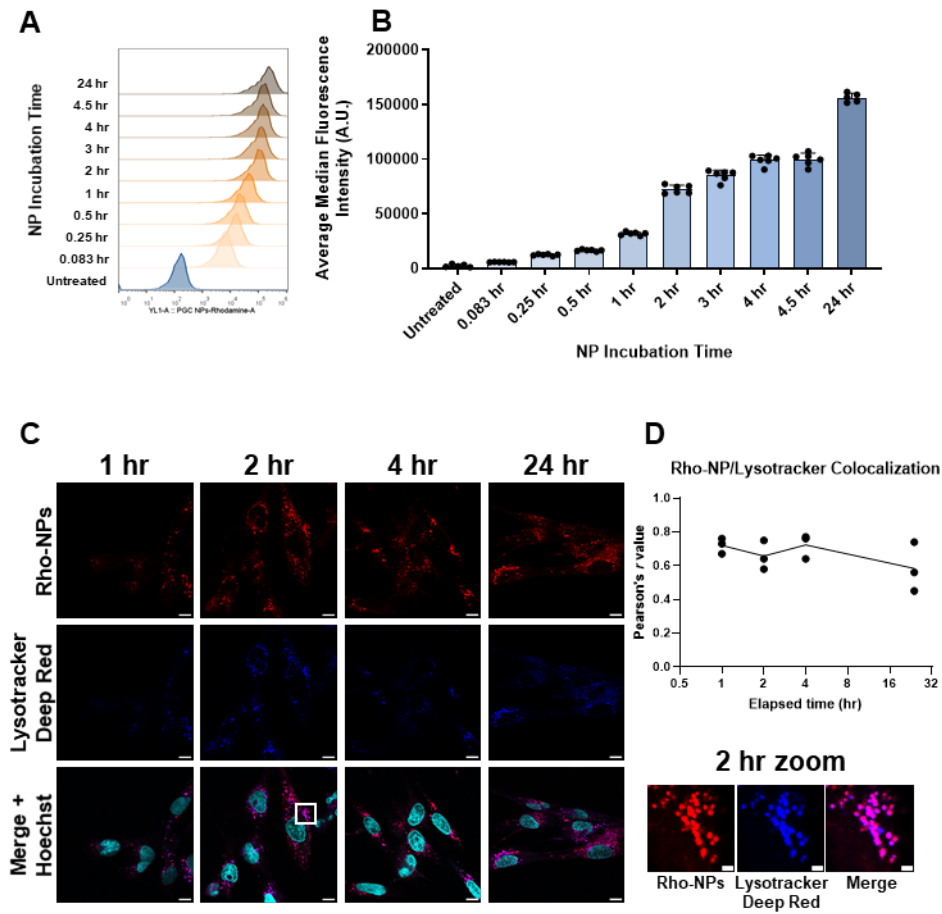


Figure 4.

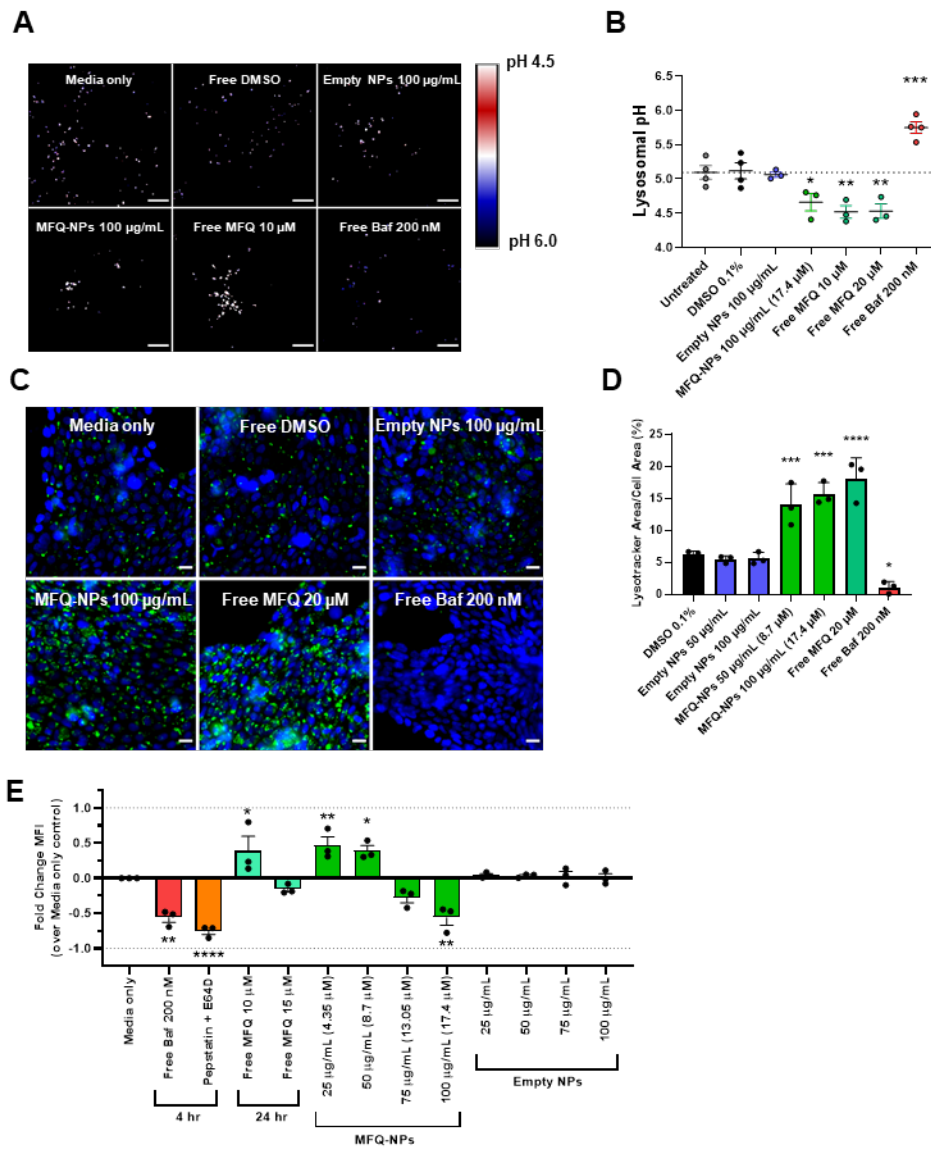


Figure 5

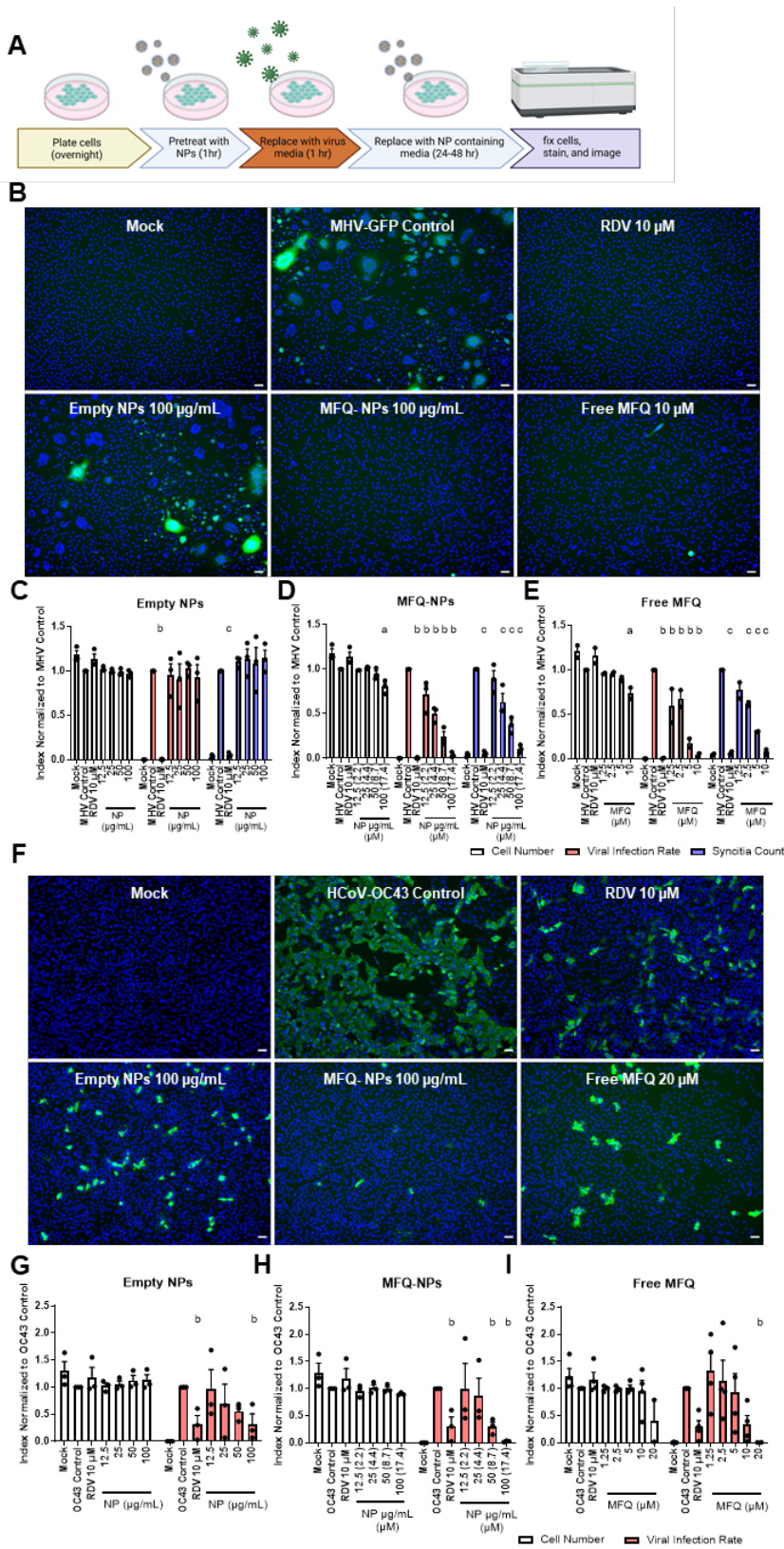
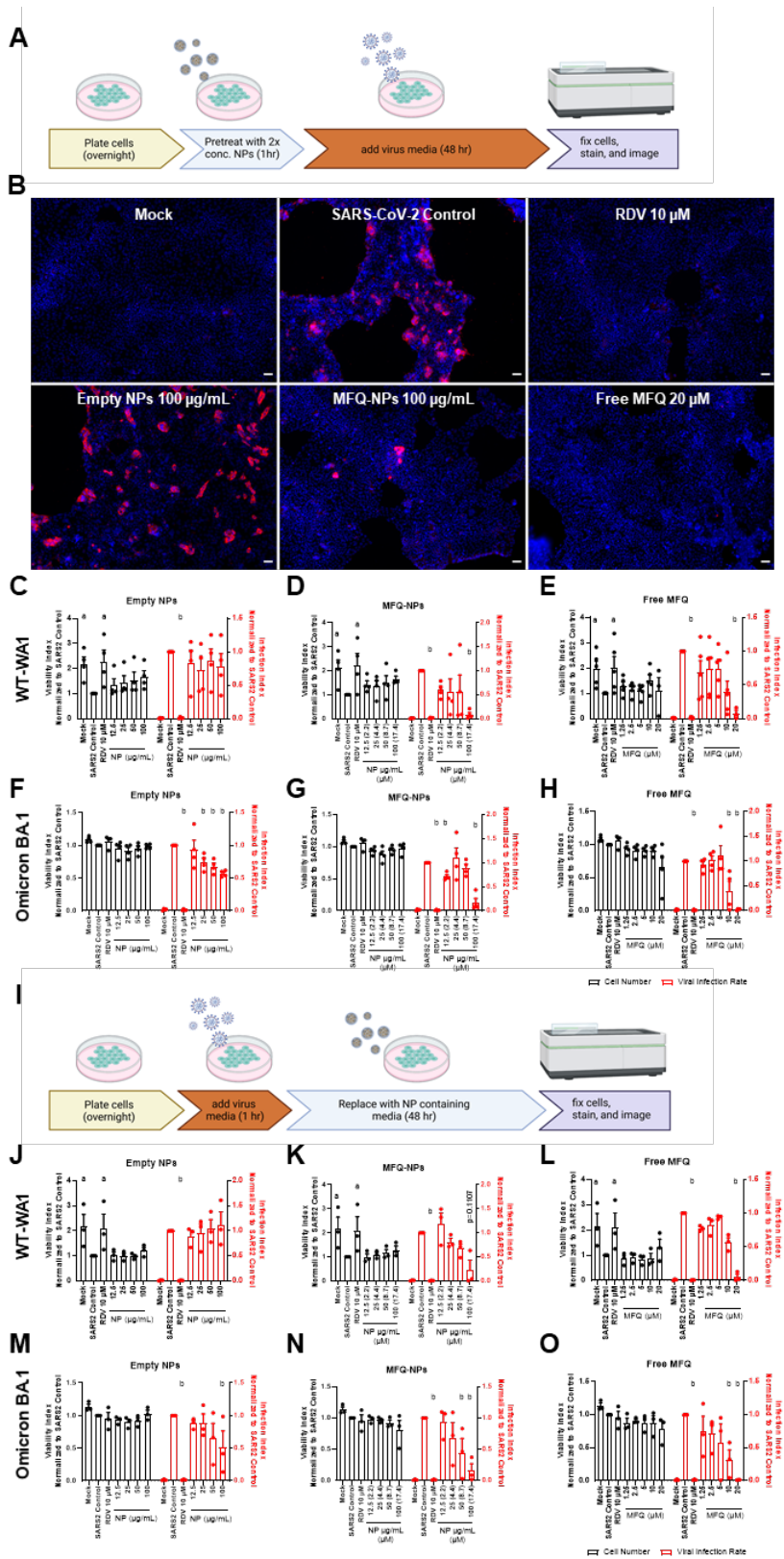
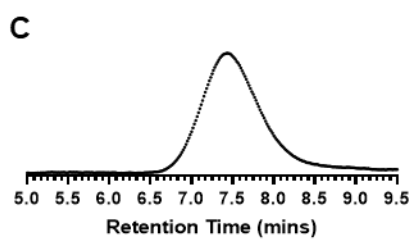
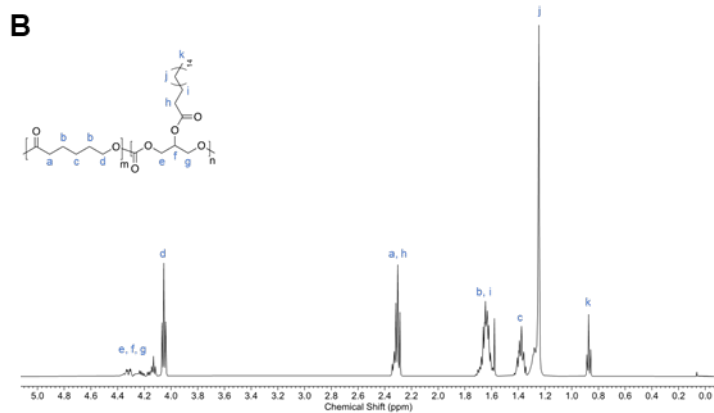
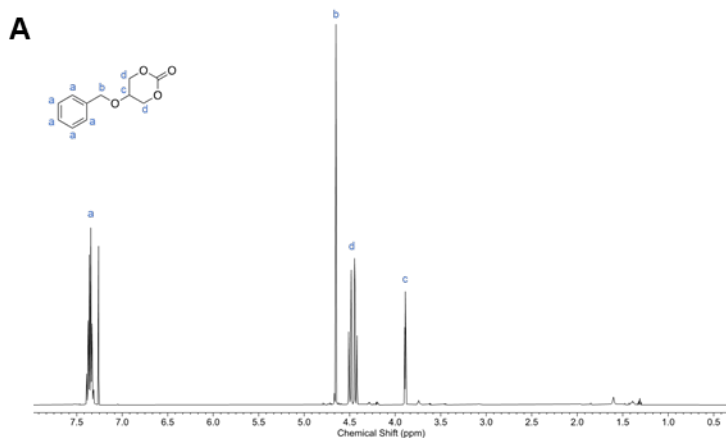


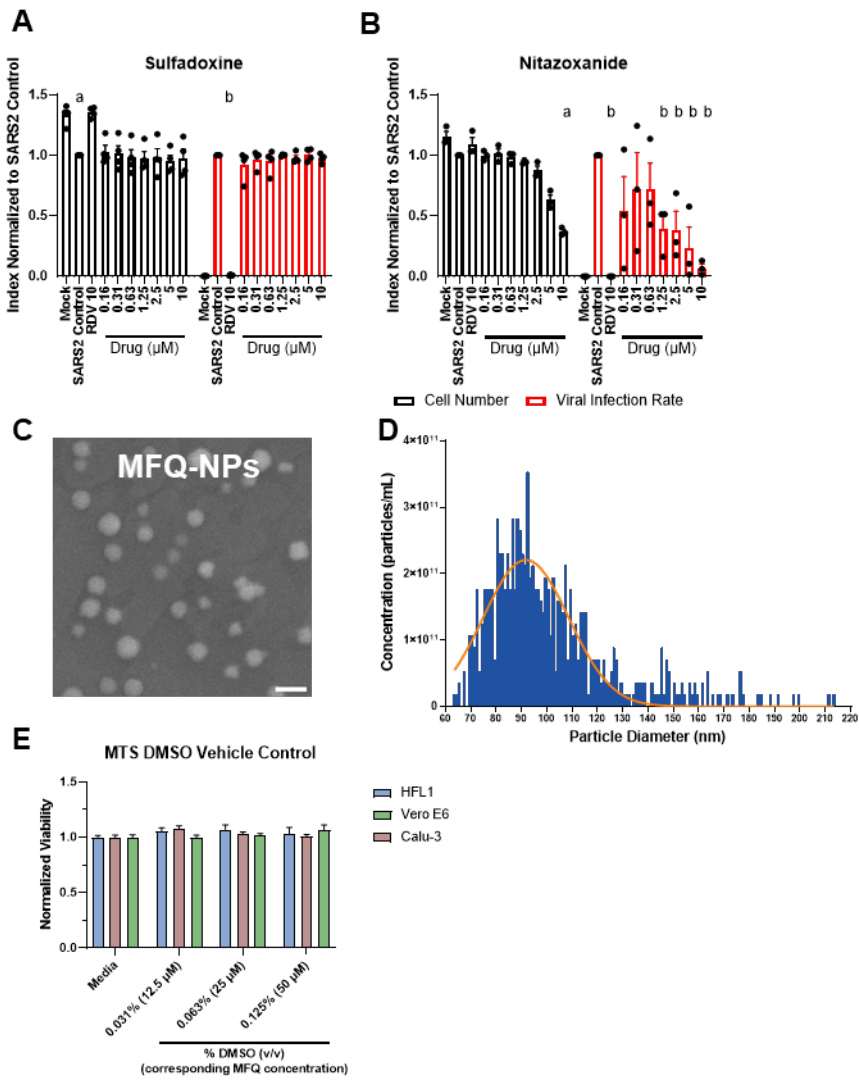
Figure 6



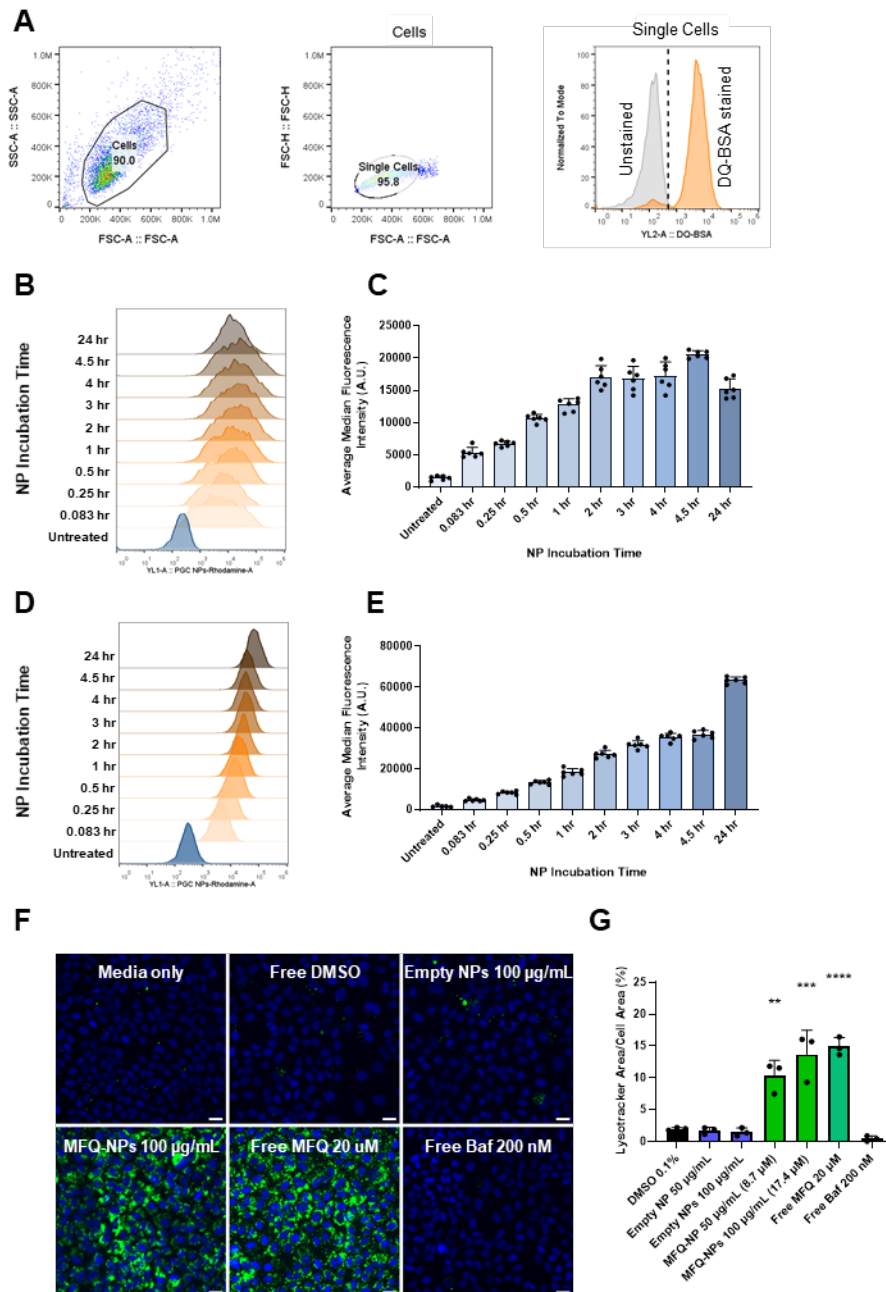
Supplemental Figure 1



Supplemental Figure 2

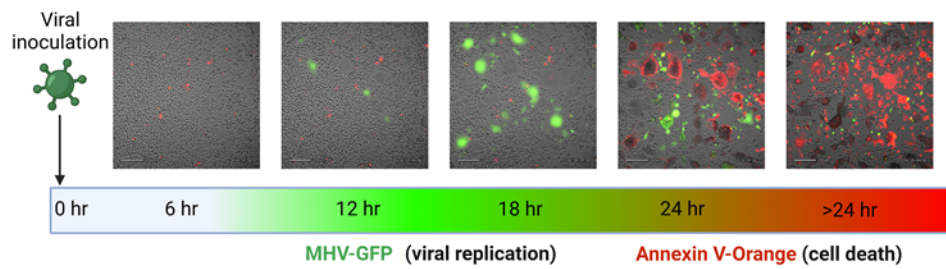


Supplemental Figure 3

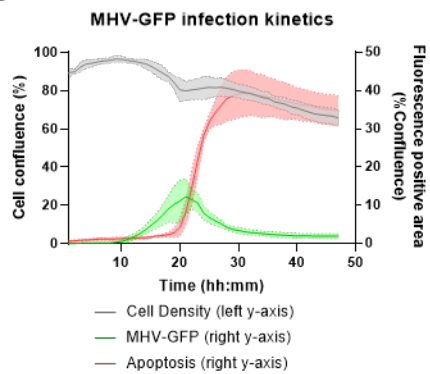


Supplemental Figure 4

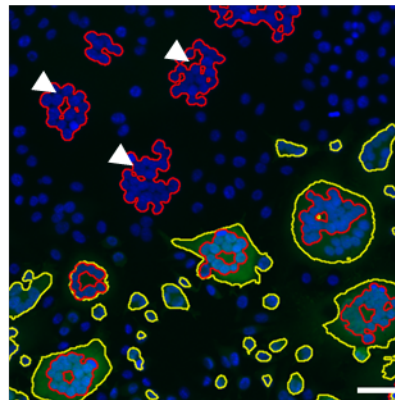
A



B



C



Supplemental Figure 5

